Mon. Not. R. Astron. Soc. **000**, 1–21 (2013) Printed 22 March 2016 (MN LATEX style file v2.2)

A path towards understanding the rotation-activity relation of M dwarfs with K2 mission, X-ray and UV data

B. Stelzer[1]⋆, M. Damasso[2], A. Scholz[3], S.P. Matt[4]
[1] *INAF - Osservatorio Astronomico di Palermo, Piazza del Parlamento 1, 90134 Palermo, Italy*
[2] *INAF - Osservatorio Astrofisico di Torino, via Osservatorio 20, 10025 Pino Torinese, Italy*
[3] *SUPA School of Physics & Astronomy, University of St. Andrews, North Haugh, St.Andrews KY 16 9SS, United Kingdom*
[4] *Department of Physics and Astronomy, University of Exeter, Physics Building, Stocker Road, Exeter, EX4 4QL, United Kingdom*

Received XXXX-XX-XX

ABSTRACT

We study the relation between stellar rotation and magnetic activity for a sample of 134 bright, nearby M dwarfs observed in the Kepler Two-Wheel (K2) mission during campaigns C0 to C4. The K2 lightcurves provide photometrically derived rotation periods, as well as various measures for activity related to cool spots and flares. We find a clear difference between fast and slow rotators with a dividing line at a period of ~ 10 d at which the activity level changes abruptly. All photometric diagnostics of activity (spot cycle amplitude, flare peak amplitude and residual variability after subtraction of spot and flare variations) display the same dichotomy, pointing to a quick transition between a high-activity mode for fast rotators and a low-activity mode for slow rotators. This unexplained behavior is reminiscent of a dynamo mode-change seen in numerical simulations that separates a dipolar from a multipolar regime. A substantial number of the fast rotators are visual binaries. This provides tentative evidence for binarity preventing spin-down and increasing activity lifetime in a way that is as yet not understood. We combine the K2 rotation periods with archival X-ray and UV data This allows us, by separating the fast from the slow rotators, to determine for the first time the X-ray saturation level separately for early- and for mid-M stars. While for K7...M4 stars the decrease of the saturation level can be attributed to the well-known mass- or luminosity- dependence of X-ray luminosity, for the coolest stars in our sample (M5...M6) there is marginal evidence for a lower $L_{\rm x}$ of saturated stars as compared to earlier M stars which needs to be corroborated with a larger sample.

Key words: stars: rotation – stars: activity – stars: flare – stars: late-type – ultraviolet: stars – X-rays: stars

1 INTRODUCTION

Together with convection, rotation is the main driver of stellar dynamos and ensuing magnetic activity phenomena (e.g. Kosovichev et al. 2013). In a feedback mechanism, magnetic fields are responsible for the spin-evolution of stars: during part of the pre-main sequence phase the magnetic field couples the star to its accretion disk dictating angular momentum transfer (Bouvier et al. 2014) and during the main-sequence phase magnetized winds remove angular momentum leading to spin-down (Kawaler 1988; Matt et al. 2015). Rotation and magnetic fields are, therefore, intimately linked and play a fundamental role in stellar evolution.

Measuring strength and topology of magnetic fields requires high-resolution spectro-polarimetry, a technique which is both time-consuming and limited to bright and fast-rotating stars (e.g. Donati & Landstreet 2009). However, how the stellar dynamo and the spin-evolution are linked can be addressed by measuring both magnetic activity and rotation rate across evolutionary timescales. While the activity-age relation is a proxy for the evolution of the stellar dynamo, the rotation-age relation discriminates between models of angular momentum evolution.

In a seminal work by Skumanich (1972) the age decay of both activity and rotation of solar-type stars was established by extrapolating between the age of the oldest known open cluster (600Myr) and the Sun (4.5Gyr). Unfortunately, stellar ages are notoriously difficult to assess. Therefore, the direct relation between rotation and activity - observed first some decades ago (e.g. Pallavicini et al. 1981; Vilhu 1984) - has widely substituted studies which involve age-estimates. The early works cited above have used spectroscopic measurements as measure for stellar rotation ($v \sin i$), and carry intrinsic ambiguities related to the unknown inclination angle of the stars. Stellar rotation rates are best derived from the periodic brightness variations induced by cool star spots moving across the line-of-sight, which can be directly associated with the rotation period.

⋆ E-mail:stelzer@astropa.inaf.it

In more recent studies of the rotation-activity connection, photometrically measured rotation periods have proven more useful than $v \sin i$.

Dynamo theory predicts a qualitative change of the dynamo mechanism (from $\alpha\Omega$ to α^2 or turbulent; Durney et al. 1993; Chabrier & Küker 2006) at the transition into the fully convective regime (spectral type $\sim$M3; Stassun et al. 2011) which may or may not result in some observable signature in the rotation – activity relation. This makes M stars particularly interesting objects for rotation-activity studies. Moreover, while improved spin-down models based on stellar wind simulations have been developed for solar-type stars (Gallet & Bouvier 2013), angular momentum evolution models of M stars are still controversial (Reiners & Mohanty 2012). Therefore, for the most abundant type of stars in our Galaxy, both the characteristics of the stellar dynamo and the angular momentum evolution are still widely elusive.

Rotation-activity studies have been presented with different diagnostics for activity, the most frequently used ones being Hα and X-ray emission. While Hα measurements are available for larger samples, especially thanks to surveys such as the *Sloan Digital Sky Survey* (e.g. West et al. 2004), X-ray emission was shown to be more sensitive to low activity levels in M dwarfs (Stelzer et al. 2013). The samples for the most comprehensive rotation-activity studies involving X-ray data have been assembled from a literature compilation, providing a large number of stars, at the expense of homogeneity. Wright et al. (2011) discuss a sample of more than 800 late-type stars (spectral type FGKM). However, the rotation-activity relation is not studied separately for M stars, possibly due to a strong bias towards X-ray luminous stars which affects especially the M stars as seen from their Fig. 5. Overall, the lack of unbiased overlapping samples with known rotation period and X-ray activity level has left the X-ray - rotation relation of M stars nearly unconstrained (see bottom right panels of Fig.5 and 6 in Pizzolato et al. 2003). Studies with optical emission lines (Hα, Ca II H&K) as activity indicator have for convenience mostly been coupled with $v \sin i$ as rotation measure because both parameters can be obtained from the same set of spectra (Browning et al. 2010; Reiners et al. 2012). Only lately has it become possible to combine Hα data with photometrically measured M star rotation periods, since a larger sample of periods have become available from ground-based planet transit search programs (West et al. 2015).

M dwarfs have not yet reached a common rotational sequence even at Gyr-ages, suggesting weaker winds and longer spin-down timescales as compared to solar-like stars (Irwin et al. 2011). The old and slowly rotating M dwarfs generally have low variability amplitudes resulting from reduced spot coverage and long rotation periods (up to months). From the ground, significant numbers of field M dwarf rotation periods have recently been measured (Newton et al. 2015). However, the sample of this study comprises only very low-mass stars ($R_* \leqslant 0.33\,R_\odot$) and seems to be incomplete in terms of the period detection efficiency (Irwin et al. 2011). The Kepler mission (Borucki et al. 2010) with its ability to provide high-precision, long and uninterrupted photometric lightcurves has led to the detection of rotation periods in > 2000 field M dwarfs (Nielsen et al. 2013; McQuillan et al. 2013, 2014), a multiple of the number known before. Interesting findings of this Kepler-study are (i) the evidence for a bimodal distribution of rotation periods for M dwarfs with $P_{\rm rot} = 0.470$ d and (ii) the fact that the envelope for the slowest observed rotation periods shifts towards progressively larger periods for stars with mass below $\sim 0.5\,M_\odot$. How these features in the rotational distribution are connected to stellar activity has not yet been examined. Most of the Kepler stars are too distant for detailed characterization in terms of magnetic activity diagnostics. However, the Kepler Two-Wheel (K2) mission is ideally suited to study both rotation and activity for nearby M stars.

Since March 2014, with its two remaining reaction wheels, the Kepler spacecraft is restricted to observations in the ecliptic plane changing the pointing direction every $\sim$ 80 d (Howell et al. 2014). With special data processing correcting for the spacecraft's pointing drift, the photometric precision of K2 is similar to that achieved by the preceding fully functional Kepler mission (Vanderburg & Johnson 2014). A great number of field M dwarfs have been selected as K2 targets with the goal of detecting planet transits. Several lists of planet candidates have already been published (e.g. Foreman-Mackey et al. 2015; Montet et al. 2015; Vanderburg et al. 2016), and some interesting planet systems have already been validated, including objects from the target list of this study (see Sect 7.8).

In our program to study the M star rotation-activity connection we limit the sample to nearby, bright M stars which provide the largest signal-to-noise in the K2 lightcurves and are most likely to be detectable at the high energies that are the best probes of magnetic activity. We derive from the K2 mission data both rotation periods and various diagnostics of magnetic activity, and we combine this with X-ray and UV activity from past and present space missions (*ROSAT*, *XMM-Newton*, *GALEX*). As mentioned above, X-ray wavelengths have proven to be more sensitive to low activity levels in M dwarfs than optical emission lines. Moreover, both X-rays and UV photons are known to have a strong impact on close-in planets, providing another motivation for characterizing the high-energy emission of these stars. Given the high occurrence rate of terrestrial planets in the habitable zone of M dwarfs ($\sim$ 50 % according to Kopparapu 2013), a substantial number of the stars we survey may soon be found to host potentially habitable worlds.

The importance of stellar magnetic activity for exoplanet studies is twofold. First, star spots and chromospheric structures introduce noise in measured radial velocity curves, so-called RV 'jitter', which depends strongly on the properties of the spots (Andersen & Korhonen 2015). Because it is an impossible task to measure the spot distribution for every potentially interesting star, relations between star spot characteristics and other activity diagnostics such as UV or X-ray emission – if applied to statistical samples – can provide useful estimates of the expected RV noise. Secondly, as mentioned above, the stellar X-ray and UV emission is crucial for the evolution and the photochemistry of planet atmospheres. While the magnetic activity of the star may erode the atmospheres of planets formed in close orbits (e.g. Penz & Micela 2008), it may by the same effect remove the gaseous envelopes of planets migrated inward from beyond the snow line and render them habitable (Luger et al. 2015). Photochemical models for planets around M dwarfs so far all rely on the UV properties of a single strongly active star, AD Leo (e.g. Segura et al. 2005; Rugheimer et al. 2015), and the lower limit of the chromospheric UV flux and its dependence on stellar parameters is not yet known. Similarly, on the high end of the activity range, with the exception of AD Leo, the frequencies and luminosities of flares on M dwarfs are still poorly constrained.

There has been significant recent progress in studies of M dwarf flares based on data from the main Kepler mission (Ramsay et al. 2013; Hawley et al. 2014; Davenport et al. 2014; Lurie et al. 2015). The time resolution of 1 min obtained in the Kepler short-cadence data proves essential for catching small events, adding to the completeness of the observed flare distributions and enabling the examination of flare morphology. The drawback is that these results are limited to individual objects or a very small group of bright stars. The K2 mission gives access to much larger samples of bright M dwarfs, for which we can examine the relation between flaring and rotation in a statistical way, albeit at lower cadence. In this work we establish, to our knowledge for the first time, a direct connection between white-light flaring and stellar rotation rate.

As described above, the sample selection is the key to success in constraining the rotation-activity relation of M dwarfs. We present our sample in Sect. 2. In Sect. 3 we derive the stellar parameters. This is necessary in order to investigate the dependence of rotation and activity on effective temperature ($T_{\rm eff}$) and mass (M_*), and to compute commonly used activity indices which consist of normalizing the magnetically-induced emission (X-ray, UV, etc.) to the bolometric luminosity. We then describe the analysis of K2 data involving the detection of flares and rotation periods (Sect. 4), archival X-ray (Sect. 5) and UV (Sect. 6) data. We present our results in Sect. 7. The implications are discussed in Sect. 8, and we provide a summary in Sect. 9.

2 SAMPLE

This work is based on all bright and nearby M dwarfs from the Superblink proper motion catalog by Lépine & Gaidos (2011, henceforth LG11) observed within the K2 mission's campaigns C0....C4. The Superblink catalog comprises an All-Sky list of 8889 M dwarfs (spectral type K7 to M7) brighter than $J = 10$, within a few tens of parsec. Many other programs focusing on M stars are carried out within the K2 mission, and rotation periods have been measured for more than a thousand M stars during the main Kepler mission (McQuillan et al. 2013). However, a careful sample selection comprising stars with already known or easily accessible magnetic activity characteristics is mandatory to nail down the rotation-activity relation. The majority of the Kepler stars are too distant (> 200 pc) and, therefore, too faint for the *ROSAT* All-Sky Survey, the main source for X-ray studies of widely dispersed samples. The proper-motion-selected M stars of the LG11 catalog are much closer and consequently brighter, facilitating the detection of both rotation periods and X-ray and UV emission.

A total of 134 Superblink M dwarfs have been observed in K2 campaigns C0...C4. Henceforth we will refer to these objects as the "K2 Superblink M star sample". The target list is given in Table 1. We list the identifier from the EPIC catalog, the campaign in which the object was observed, the designation from the *Third Catalog of Nearby Stars* (CNS 3; Gliese & Jahreiß 1991), magnitudes in the Kepler band and further parameters, the calculation of which is described in the next section.

3 FUNDAMENTAL STELLAR PARAMETERS

We derive physical parameters of the K2 Superblink M stars (effective temperature, mass, radius, and bolometric luminosity) by adopting empirical and semi-empirical calibrations from Mann et al. (2015), which are based on the color indices $V-J$ and $J-H$, and on the absolute magnitude in the 2 MASS K band, $M_{\rm K_S}$. The calibrations of Mann et al. (2015) are valid for dwarf stars, and can be expected to hold for the K2 Superblink M star sample which has been cleaned by LG 11 from contaminating giants. Due to a press error some wrong values appeared in the tables of Mann et al. (2015). We use here the correct values reported in the erratum[1].

[1] http://iopscience.iop.org/article/10.3847/0004-637X/819/1/87/meta

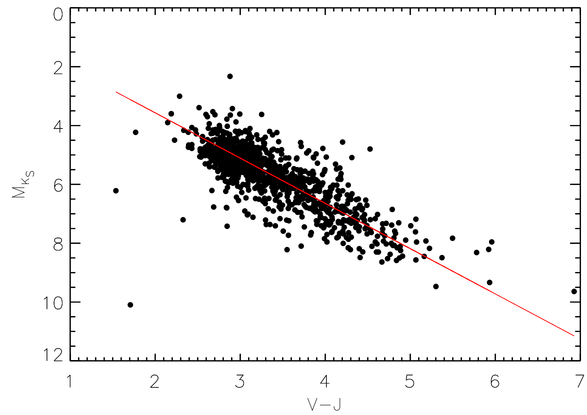

Figure 1. Calibration of the linear relation between absolute $K_{\rm S}$ magnitude, $M_{\rm K_S}$, and $V-J$ color obtained from a sample of $1,078$ M dwarfs with measured trigonometric parallax in LG11 (black circles). Our best-fit model is represented by a red solid line. The residuals have a scatter of 0.56 mag.

Stellar magnitudes and their uncertainties are obtained from the UCAC4 catalog (Zacharias et al. 2013) which provides 2MASS near-IR photometry and V band magnitudes from *The AAVSO Photometric All Sky Survey (APASS)*; Henden & Munari (2014). These latter ones are more accurate and have significantly better precision than the V band magnitudes given in LG 11. For the 6 stars with no V magnitude in UCAC4, we found measurements in Data Release 9 of the APASS catalog[2].

We derive an empirical linear calibration to calculate $M_{\rm K_S}$ for our sample, using a list of $1,078$ M dwarfs with apparent $K_{\rm S}$ magnitude from UCAC 4 and trigonometric parallax in LG 11. The best linear least-squares fit to the data is obtained through a Monte-Carlo analysis. This approach provides more realistic errors than simple least-squares fitting because the uncertainties are derived from posterior distributions of the parameters and take into account all the errors affecting the measurements.

Specifically, we generate $10,000$ synthetic samples (each composed of $1,078$ stars) drawing $V-J$ and $M_{\rm K_S}$ randomly from 2D normal distributions with mean equal to the observed values and standard deviation (henceforth STD) equal to the uncertainties. We then fit to each of the $10,000$ representations a straight line with the IDL[3] `FITEXY` routine, assuming for each simulated point the original errors in both variables. The best-fit relation is then defined by the median values and standard deviations of the *a posteriori* Monte-Carlo distribution for the coefficients in the linear fit, given by

$$M_{\rm K_S} = 0.49(\pm 0.02) + 1.539(\pm 0.006) \cdot (V-J) \qquad (1)$$

The residuals of this solution, which is applicable in the range $1.54 < V-J < 6.93$, show a rms of 0.56 mag. In Fig. 1 we show this relation overplotted on the observed data.

All other stellar parameters and their uncertainties are calculated in the same manner through a Monte-Carlo analysis. In particular, the stellar effective temperatures ($T_{\rm eff}$) are obtained from the calibration relation which uses $V-J$ and $J-H$ (Eq. 7 in Mann et al. 2015), while radii (R_*) and masses (M_*) are calculated from

[2] https://www.aavso.org/apass

[3] IDL is a product of the Exelis Visual Information Solutions, Inc.

relations with $M_{\rm K_S}$ (Eqs. 4 and 10 in Mann et al. 2015, respectively), and the bolometric correction $BC_{\rm K}$ is derived through a third-degree polynomial with $V-J$ as independent variable (presented in Table 3 of Mann et al. 2015).

Thus, we first generate for each star a sample of $10,000$ synthetic $V-J$, $J-H$, and $M_{\rm K_S}$ datasets drawn from normal distributions with mean and sigma equal to the observed value and its error. Then we apply to each star the above-mentioned calibrations from Mann et al. (2015). The best estimate of each parameter ($T_{\rm eff}$, R_*, M_* and $BC_{\rm K}$) is then obtained as the median value of the corresponding *a posteriori* distribution, with its standard deviation assumed as the uncertainty.

To provide conservative estimates of the stellar parameters, the uncertainties representing the scatter of the relations of Mann et al. (2015, see Tab. 1, 2, and 3 therein) are propagated into the Monte-Carlo process. Specifically, for $T_{\rm eff}$ we consider the scatter in the difference between the predicted and the spectroscopically observed temperature (48 K), and the typical uncertainty on the spectroscopic value of $T_{\rm eff}$ (60 K) adding both in quadrature, while for $BC_{\rm K}$ we consider the uncertainty of 0.036 mag. These additional uncertainties are taken into account in the Monte-Carlo analysis when drawing randomly the samples. For radius and mass, Mann et al. (2015) provide relative uncertainties of 2.89 % and 1.8%, respectively. These values are calculated from the median values of our posterior distributions for R_* and M_* and are then added in quadrature to their standard deviations.

Mann et al. (2015) argue that some of the above-mentioned relations for the stellar parameters can be improved by including an additional term involving metallicity ([Fe/H]). We found [Fe/H] measurements in the literature (Newton et al. 2014) for only 6 stars from the K2 Superblink M star sample, and we verified for these objects that the radii and temperatures derived by taking account of [Fe/H] (Eqs. 5 and 6 in Mann et al. 2015) are compatible with our estimates described above.

From $BC_{\rm K}$ and $M_{\rm K_S}$ we calculate the absolute bolometric magnitudes of our sample, which are then converted into luminosities assuming the absolute bolometric magnitude of the Sun is $M_{\rm bol,\odot} = 4.7554$. We note, that the distances we infer from our $M_{\rm K_s}$ values and the observed K_s magnitudes are systematically larger, on average by about ~ 30 %, than the photometric distances presented by LG11 for the same stars. In the near future, *Gaia* measurements will provide the ultimate and accurate distances for all K2 Superblink M stars. In the meantime, our estimates, which are based on the most accurate photometry available to date, can be considered as a best guess on the distances.

All stars in the K2 Superblink M star sample have a photometric estimate of the spectral type in LG 11, based on an empirical relation of spectral type with $V-J$ color which was calibrated with SDSS spectra. Since we use here the higher-precision UCAC 4 V band magnitudes, for consistency with our calculation of the other stellar parameters, we derive an analogous relation between $V-J$ and spectral type. To this end, we make use of $1,173$ stars classified as K7 or M-type dwarfs by Lépine et al. (2013) based on spectroscopy. We group the stars in bins of 0.5 spectral subclasses, with K7 corresponding to -1, M0 to 0, and so on until M4.5, which is the last sub-type for which we have enough stars in the calibration sample for a useful fit. We calculate the mean and standard deviation of $V-J$ for each spectral type bin, and notice that the data can be fitted with a combination of two straight lines for the ranges [K7,M2] and [M2,M4.5] (see Fig. 2). Our fit, performed through a

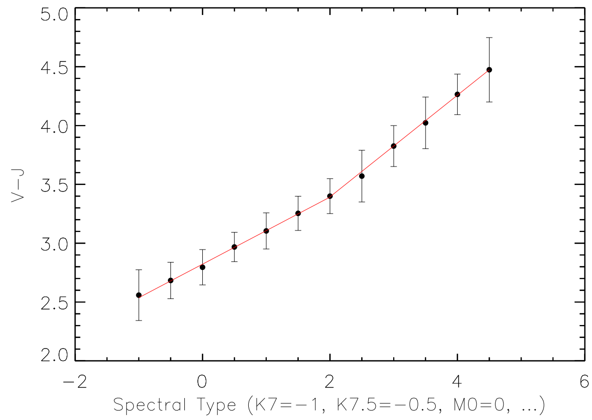

Figure 2. Calibration of the relation between spectral type and $V-J$ obtained from a sample of $1,173$ M dwarfs with spectroscopically determined spectral type in Lépine et al. (2013). We fit the data with two straight lines (red solid lines), one for stars with sub-types earlier than M2 and the other one for those with sub-types later than M2.

Monte-Carlo procedure as described above, results in the relations

$$V-J = 2.822(\pm0.067) + 0.285(\pm0.061)\cdot SpT \quad (2)$$

$$V-J = 2.53(\pm0.29) + 0.432(\pm0.093)\cdot SpT \quad (3)$$

which are valid for $2.5 \leqslant V-J \leqslant 3.4$ and $3.4 \leqslant V-J \leqslant 4.5$, for the hotter (Eq. 2) and cooler (Eq. 3) spectral types respectively. We use this calibration to classify the K2 Superblink M star sample, by rounding the results of the linear relations to the closest spectral sub-type. Nine K2 Superblink M stars have $V-J$ colors slightly beyond the boundaries for which we calibrated Eqs. 2 and 3 and we extrapolate the relations at the ends to spectral types K5 and M5, respectively. No star deviates by more than 0.5 spectral subclasses from Eqs. 2 and 3. The spectroscopically determined spectral types from the literature, which are available for roughly three dozens of the K2 Superblink M stars, are in excellent agreement with our values (see Reid et al. 2004; Reiners et al. 2012; Lépine et al. 2013).

In Table 1 we provide the photometry (Kepler magnitude $K_{\rm p}$, V, J, and $K_{\rm s}$), the distances obtained from the absolute K band magnitude, the fundamental parameters (M_*, R_*, $\log L_{\rm bol}$ and $T_{\rm eff}$) and the spectral type (SpT) derived as described above. The few stars with $M_{\rm K_S}$ slightly more than $3\,\sigma$ smaller than the lower boundary of the calibrated range ($4.6 < M_{\rm K_s} < 9.8$) are flagged with an asterisk in Table 1.

Stars for which the K2 photometry – and in some cases also the optical/IR photometry used by us to calculate the stellar parameters – comprises a potential contribution from a close binary companion are discussed in detail in the Appendix A. These stars are also highlighted in Table 1 and flagged in all figures where relevant. The Gl 852 AB binary is represented in our target list by two objects (EPIC 206262223 and EPIC 206262336) but they are not resolved in the K2 aperture[4], i.e. only the combined lightcurve of both stars is at our disposition. We compute the stellar parameters for both components in the binary using the individual V magnitudes from Reid et al. (2004); then we assign the rotational pa-

[4] Our analysis relies on the data reduction performed by A.Vanderburg; see Sect. 4.

rameters and the X-ray/UV emission to the brighter, more massive star (EPIC 206262336) and we do not consider the secondary (EPIC 206262223) any further.

The distributions of spectral type and mass for the K2 Superblink M star sample are shown in Fig. 3. Covering spectral type K5 to M5 (masses between about 0.2 and $0.9\,M_{\odot}$), this is an excellent database for investigating the connection between rotation and activity across the fully convective boundary (SpT ∼M3/M4).

4 K2 DATA ANALYSIS

We base our analysis of K2 time-series mostly on the lightcurves made publicly available by A.Vanderburg (see Vanderburg & Johnson 2014, and Sect. 4.1). We use the "corrected" fluxes in which the features and trends resulting from the satellite pointing instability have been eliminated. All stars of the K2 Superblink M star sample have been observed in long-cadence (LC) mode with time-resolution of $\Delta t = 29.4$ min. Nine stars have in addition short-cadence (SC) data available ($\Delta t = 1$ min). In the following, where not explicitly stated, we refer to the LC data.

Our analysis comprises both the measurement of rotation periods and an assessment of photometric activity indicators. In particular, the identification of flares is of prime value both for activity studies and for obtaining a "cleaned" lightcurve allowing to perform more accurate diagnostics on the rotation cycle, e.g. its amplitude. The main limitation of the LC data is the difficulty in identifying short-duration flares, as a result of poor temporal resolution combined with remaining uncertainties on the quality of the photometry. However, in this work we aim at elaborating trends between activity and rotation, and for this purpose completeness of the flare sample is less important than having statistically meaningful numbers of stars.

Rotation and activity diagnostics are determined with an iterative process in which we identify "outliers" in the K2 lightcurves. This involves removing any slowly varying signal by subtracting a smoothed lightcurve from the original data. The appropriate width of the boxcar in the smoothing process depends on the time-scale of the variation to be approximated, i.e. on the length of the rotational cycle. Therefore, we start the analysis with a first-guess period search on the original, corrected lightcurve. We use three methods to determine rotation periods which are laid out in Sect. 4.4. Before presenting the details of our period search we describe how we prepare the lightcurves and how we extract the flares and "clean" the corrected lightcurves further, thus removing both astrophysical flare events and residual noise from the data reduction.

4.1 Data preparation

We download the lightcurves reduced and made publicly available by A. Vanderburg[5]. The data reduction steps are described by Vanderburg & Johnson (2014). In short, the authors extracted raw photometry from K2 images by aperture photometry. The variability in the resulting lightcurves is dominated by a zigzag-like pattern introduced by the instability of the satellite pointing and its correction with help of spacecraft thruster fires taking place approximately every 6 h. This artificial variability can be removed by a "self-flat fielding" process described in detail by Vanderburg & Johnson (2014). We base our analysis on these "corrected" or "detrended" lightcurves to which we apply some additional corrections.

Upon visual inspection of each individual corrected lightcurve we notice some flux jumps. As explained by A.Vanderburg in his data release notes[6] such offsets can arise due to the fact that he divides the lightcurves in pieces and performs the data reduction separately on each individual section. In stars with long-term variations these offsets are clearly seen to be an artefact of the data reduction, and we remove them by applying a vertical shift to the lightcurve rightwards of the feature. Note that, since the absolute fluxes are irrelevant for our analysis it does not matter which side is used as the baseline for the normalization. While such flux jumps are evident in lightcurves with slow variations, for stars with short periods it is much more difficult to identify such systematic offsets and even if they are identified it is impossible to perform the normalization without *a priori* knowledge of the (periodic) variation pattern. However, since such short-period lightcurves comprise many rotational cycles, the period search is much less sensitive to such residual artifacts than it is for long-period lightcurves.

In a second step, we remove all cadences in which the satellite thrusters were on (and the telescope was moving). Several lightcurves have spikes and decrements produced by incomplete background removal or individual null values among the fluxes. We identify such obvious artefacts by visual inspection of each individual lightcurve and remove the respective data points. We then fill all gaps in the K2 lightcurves, i.e. all data points separated by multiples of Δt, by interpolation on the neighboring data points. Evenly spaced data is required for the auto-correlation function, one of the methods we use for the period search (see Sect. 4.4.1). We add Gaussian noise to the interpolated data points. To avoid that the width of the distribution from which the errors are drawn is dominated by the rotational variation we use only the nearest data points to the right and to the left of the gap to define mean and sigma of the Gaussian.

4.2 Identification of flares

Then we start the iterative flare search and cleaning process which consists in (i) boxcar smoothing of the lightcurve, (ii) subtraction of the smoothed from the original lightcurve (i.e. removal of the rotational signal), and (iii) flagging and removal of all data points which deviate by more than a chosen threshold from the subtracted curve. We repeat this procedure three times with successively smaller width of the boxcar. Subsequently, the removed cadences are re-generated by interpolation and addition of white noise as described above. This provides a lightcurve that is free from flares (henceforth referred to as the "cleaned" lightcurve). When subtracted from the original corrected data, the result is a flat lightcurve (henceforth referred to as the "flattened" lightcurve) in which the rotational variation has been removed and the dominating variations are flares, eclipses and artefacts.

A significant fraction of the data points that have been removed in the above σ-clipping process are isolated cadences. Such events are found both as up- and downward excursions in the flattened lightcurves. The number of upward outliers is for most lightcurves much larger than the number of downward outliers, suggesting that many of these events are genuine flares. However, we

[5] The reduced K2 lightcurves were downloaded from https://www.cfa.harvard.edu/∼avanderb/k2.html

[6] The technical reports on the detrending process carried out by A.Vanderburg are accessible at https://www.cfa.harvard.edu/∼avanderb/k2.html

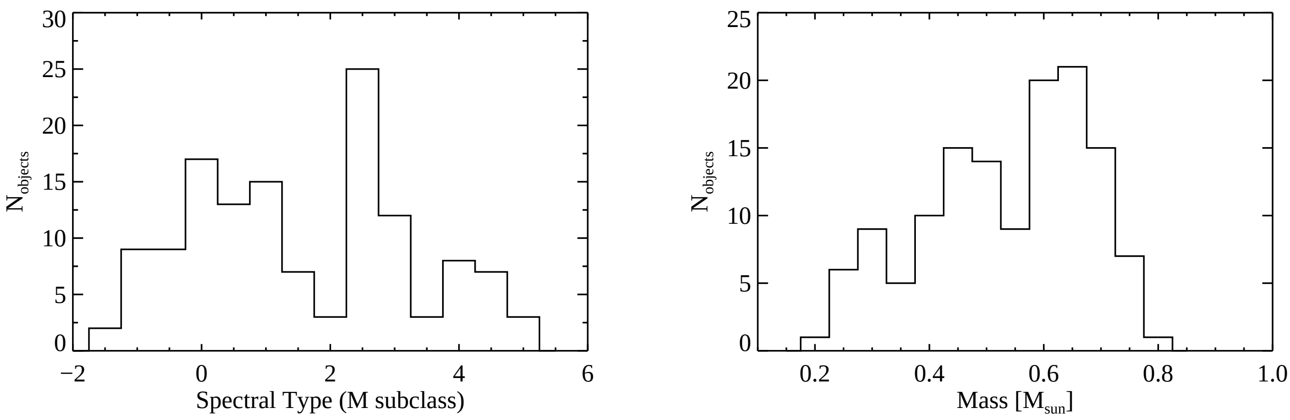

Figure 3. Distribution of spectral types and masses for the K2 Superblink M star sample observed in campaigns C0 to C4. Negative indices denote spectral types earlier than M, where the value -1 stands for K7. See text in Sect. 3 for details.

[t]

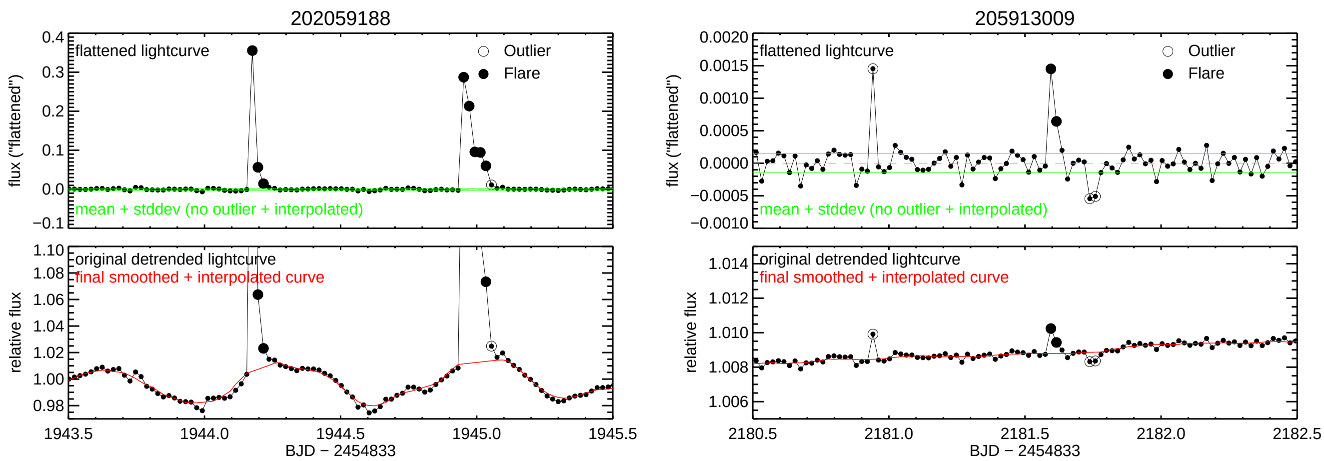

Figure 4. Examples of lightcurves illustrating the procedure applied to identify flares; see text in Sect. 4.2 for details.

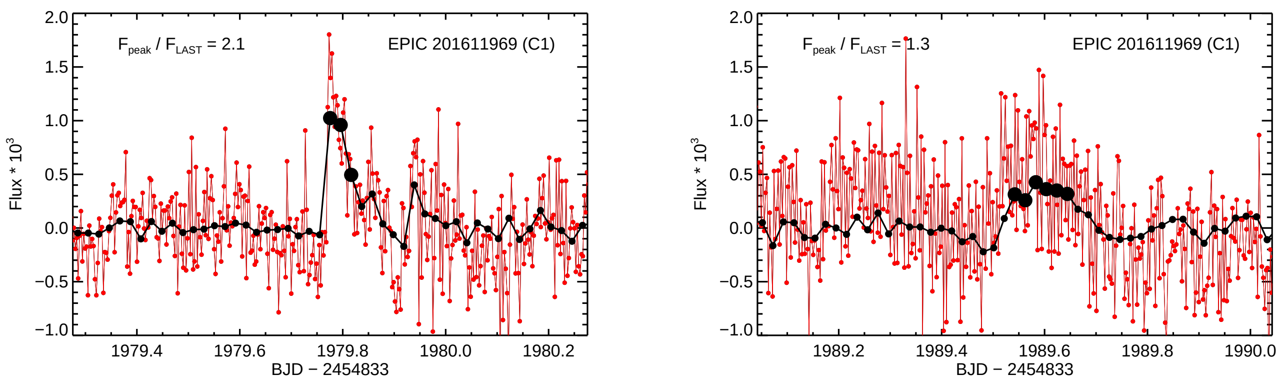

Figure 5. Portion of the long-cadence (black) and short-cadence (red) K2 lightcurve for EPIC 201611969. Flare candidates in LC data according to criteria (i) - (iv) described in Sect. 4.2 are marked with large filled circles; bins with interpolated data are high-lighted with large diamonds. On the left a bona-fide flare, on the right a flare candidate which we discard on the basis of its shape ($F_{\rm peak}/F_{\rm last} < 2$). The SC lightcurve has been binned to a cadence of $4\,s$; any vertical offset is the result of the different analysis for SC and LC data and is irrelevant for our purpose of comparison the shape of flare candidates.

Table 1: Target list for K2 Campaign C0...C4 with stellar parameters.

EPIC ID	Campaign	CNS-name	K_p [mag]	V [mag]	J [mag]	K_s [mag]	d [pc]	M_* [$M_\odot$]	R_* [$R_\odot$]	$\log L_\mathrm{bol}$ [$L_\odot$]	T_eff [K]	SpT
202059188[B]	C0		14.70	14.32 ± 0.05	9.88 ± 0.02	9.04 ± 0.02	22.0	0.27 ± 0.01	0.27 ± 0.01	-2.13 ± 0.04	3181 ± 80	M4.5
202059192	C0		13.10	13.09 ± 0.02	9.99 ± 0.02	9.15 ± 0.02	59.9	0.59 ± 0.01	0.56 ± 0.02	-1.23 ± 0.03	3712 ± 80	M1.0
202059193	C0		12.50	12.42 ± 0.03	9.54 ± 0.02	8.71 ± 0.02	57.2	0.65 ± 0.02	0.63 ± 0.02	-1.08 ± 0.03	3835 ± 82	M0.0
202059195	C0	G 103-029	14.70	14.18 ± 0.06	9.95 ± 0.02	9.07 ± 0.02	25.9	0.31 ± 0.01	0.31 ± 0.01	-1.99 ± 0.05	3306 ± 81	M4.0
202059198	C0		11.60	11.62 ± 0.02	8.48 ± 0.06	7.65 ± 0.02	29.2	0.58 ± 0.02	0.55 ± 0.02	-1.26 ± 0.05	3724 ± 99	M1.0
202059199	C0	LP 420-6	12.60	12.60 ± 0.02	9.06 ± 0.02	8.22 ± 0.03	28.6	0.47 ± 0.01	0.45 ± 0.02	-1.53 ± 0.03	3533 ± 83	M2.5
202059203	C0	LP 362-257	14.10	13.64 ± 0.03	9.71 ± 0.02	8.81 ± 0.02	28.5	0.38 ± 0.01	0.37 ± 0.01	-1.79 ± 0.03	3414 ± 79	M3.0

[B] Potential contamination by companion star in binary (see Appendix A).

[*] M_Ks slightly outside the range of calibrated values (see text in Sect. 3).

[a] This star (Gl 852B) is not considered further because we assign the rotation and activity to the primary (Gl 852A) in the unresolved binary.

The full table is available in the electronic edition of the journal.

assume here a conservative approach aimed at avoiding counting spurious events as flare. Therefore, we select all groups of at least two consecutive upwards deviating data points as flare candidates. In practice, this means that the minimum duration of the recognized flares is ~ 1 hr (two times the cadence of 29.4 min). We additionally impose that, in order to be selected as bona-fide flare, the cadence representing the observed peak of the flare ($F_{\rm peak}$) must have a significance of $\geqslant 3\,\sigma$. We measure this with respect to the mean and standard deviation of the flattened lightcurve from which outliers have been removed, which is defined and further discussed in Sect. 4.3. Finally, we require that $F_{\rm peak}$ must be at least twice the flux of the last of the data points defining the flare ($F_{\rm last}$). As shown below, this last criterion removes "flat-topped" events from our list of bona-fide flares which we trust less than "fast-decay" events given the possibility of residual artifacts from the data acquisition and reduction.

A zoom into two examples of LC lightcurves with flares is shown in Fig. 4 and illustrates our flare search algorithm. The lower panel shows the original, detrended lightcurve and overlaid (in red) the smoothed lightcurve. The upper panel shows the result from the subtraction of these two curves, i. e. the flattened lightcurve. We highlight data points regenerated through interpolation (open diamonds), data points identified as outliers (open circles), and data points that belong to bona-fide flares (filled circles). The example on the right demonstrates the inability of recognizing short flares with our detection procedure. Short-cadence data from the main Kepler mission have shown that many flares on active M stars are, in fact, significantly shorter than one hour (see e.g. Hawley et al. 2014). SC lightcurves are available for 9 stars from the K2 Superblink M star sample. The analysis of SC lightcurves will be described elsewhere. In this work we use the SC data only as a cross-check on the quality of our flare search criteria applied to the LC data (see below and Fig. 5). We recall that we aim at a conservative approach, avoiding at best possible spurious events in the flare sample, because our aim is to study trends with rotation.

To summarize, the parameters of our flare search algorithm are (i) the width of the boxcar [adapted individually according to the first-guess period], (ii) the threshold for outliers identified in the σ-clipping process [adopted to be $3\,\sigma$], (iii) the minimum number of consecutive data points defining a flare [2], (iv) the significance of the flare peak flux $F_{\rm peak}$ [$3\,\sigma$], and (v) the flux ratio between the flare peak bin and the last flare bin [$F_{\rm peak}/F_{\rm last} \geqslant 2$]. The values for these parameters have been chosen by testing various combinations of criteria (i) - (v) with different parameter values and comparing the results to a by-eye inspection of the "flattened" lightcurves. In particular, criterion (v) is introduced after a comparison of LC and SC lightcurves which shows that, generally, the LC flare candidates correspond to analogous features in the SC data but in some cases the features are very different from the canonical flare shape (characterized by fast rise and exponential decay). Fig. 5 demonstrates that with criterion (v) we de-select such broad events from the list of bona-fide flares: Two flare candidates according to criterion (i) - (iv) are shown; the event on the left panel is a bona-fide flare according to criterion (v) while the event on the right does not fullfill $F_{\rm peak}/F_{\rm last} \geqslant 2$.

4.3 Residual variability and photometric noise

In Fig. 6 we show the standard deviations of the flattened lightcurves, $S_{\rm flat}$, for two cases: including and excluding the data points identified as outliers. The 'outliers' comprise flares, transits or eclipses, and artefacts from the data reduction. Therefore,

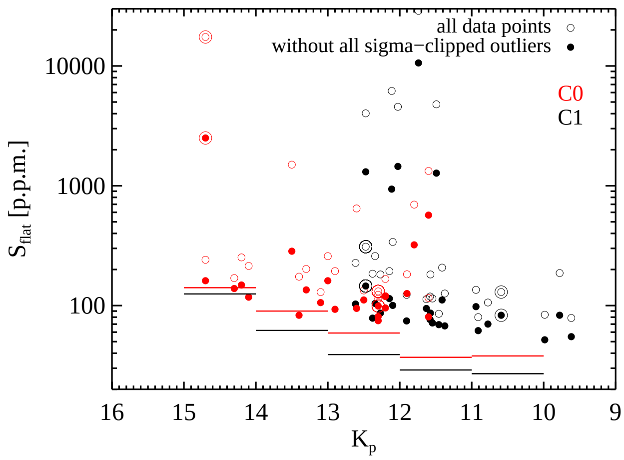

Figure 6. Standard deviation for the lightcurves of the Superblink stars observed in campaign C0 and C1 after "flattening" by removal of the rotational signal as described in Sect. 4.2. $K_{\rm p}$ is the magnitude in the Kepler band. The STD of the subtracted lightcurve is calculated for two data sets: the full lightcurve (open circles) and the lightcurve without all data points that were identified as outliers during the clipping process (filled circles). Horizontal lines represent the 6 hr-precisions for C0 and C1 calculated by A.Vanderburg (see footnote to Sect.4.1) for a sample of cool dwarfs drawn from different K2 Guest Observer programs. Stars with a possible contribution in the K2 photometry from an unresolved binary companion are highlighted with large annuli.

the case without outliers (red data points) the standard deviation is calculated on the residual lightcurve from which the known astrophysical sources of variability have been removed, and it can be expected to represent the noise level in our data.

We restrict Fig. 6 to campaigns C0 and C1 for which the data release notes of A.Vanderburg (see footnote to Sect. 4.1) provide an estimate of the 6 hr-precision based on a sample of cool dwarfs that is not clearly specified. Our $S_{\rm flat}$ measurements suggest a somewhat lower precision for the K2 Superblink M star sample. This might be due to differences in the definitions. Vanderburgs's 6 hr-precisions are medians for their sample and the scatter among their stars is much larger than the factor two difference with our $S_{\rm flat}$ values. Also, we measure the standard deviation on the full lightcurve while Vanderburg's precisions are based on a running 6 hr mean. An alternative explanation for the apparently different photometric precisions could lie in different activity levels of the two samples, implying residual fluctuations of astrophysical origin in our "noise". In fact, in Sect. 7.3 we present evidence that $S_{\rm flat}$ comprises an astrophysical signal. Overall, our analysis presented in Fig. 6 confirms the high precision achieved in K2 lightcurves with the detrending method applied by A.Vanderburg.

4.4 Period search

We explore multiple approaches to measure rotation periods on the K2 data.

4.4.1 Period search on detrended lightcurves

We apply standard time-series analysis techniques, the Lomb Scargle (LS) periodogram and the auto-correlation function (ACF), to the detrended K2 lightcurves made publicly available (see Vanderburg & Johnson 2014). As mentioned in Sect. 4, as a first step we perform the period search directly on the corrected version of the downloaded lightcurves with the purpose of adapting the boxcar width in the course of the search for flares. We then repeat the period search on the "cleaned" lightcurves obtained after the σ-clipping process and the regeneration of the missing data points through interpolation, i.e. after removal of the flares and other outliers. The analysis is carried out in the IDL environment using the SCARGLE and A_CORRELATE routines.

Periodograms and ACFs have already been used successfully to determine rotation periods in Kepler data (e.g. McQuillan et al. 2013; Nielsen et al. 2013; Rappaport et al. 2014; McQuillan et al. 2014). As a cross-check on our procedure, we have downloaded Kepler lightcurves from the *Mikulski Archive for Space Telescopes* (MAST)[7] for some M stars from the McQuillan et al. (2013) sample and we have verified that we correctly reproduce the published periods.

Following McQuillan et al. (2013), in our use of the ACF method we generally identify the rotation period as the time lag, $k \cdot \Delta t$ with integer number k, corresponding to the first peak in the ACF. Subsequent peaks are located at multiples of that period, resulting in the typical oscillatory behavior of the ACF. Exceptions are double-peaked lightcurves where the ACF presents two sequences of equidistant peaks (see e.g. Fig. 7). Such lightcurves point to the presence of two dominant spots, and we choose the first peak of the sequence with higher ACF signal as representing the rotation period. McQuillan et al. (2013) have performed simulations that demonstrate the typical pattern of the ACF for different effects in the lightcurve, such as changing phase and amplitude, double peaks, and linear trends. All these features are also present in the K2 data, although less pronounced than in the much longer main Kepler mission time-series examined by McQuillan et al. (2013).

The classical periodogram is based on a Fourier decomposition of the lightcurve. In the form presented by Scargle (1982), it can be applied to unevenly sampled data and is essentially equivalent to least-squares fitting of sine-waves. Realistic time-series deviate from a sine-curve, and are subject to the effects described above. This introduces features in the power spectrum. Since the dominating periodicity in the K2 Superblink stars is reasonably given by the stellar rotation cycle, the highest peak of the periodogram can be interpreted as representing the rotation period. The LS-periodograms are computed here for a false-alarm probability of 0.01 using the fast-algorithm of Press & Rybicki (1989).

In Fig. 7 we show an example for a detrended K2 lightcurve, its LS-periodogram and ACF, and the lightcurve folded with the derived period.

4.4.2 Period search on un-detrended lightcurves

As an independent check we derive the stellar rotation periods with the Systematics-Insensitive Periodogram (SIP) algorithm developed by Angus et al. (2015), that produces periodograms calculated from the analysis of the raw K2 photometric time series. For each observing campaign, these are modelled with a linear combination of a set of 150 'eigen light curves' (ELC), or basis functions, that describe the systematic trends present in K2 data, plus a sum of sine and cosine functions over a range of frequencies[8]. For each test frequency, the system of linear equations is solved through a least-square fit to the data. The periodogram power is determined as described in Angus et al. (2015), by calculating the squared signal-to-noise ratio *(S/N)*^{2} for each frequency. *(S/N)*^{2} is a function of the sine and cosine coefficients (i.e. the amplitudes), where the frequencies corresponding to amplitudes not well constrained by the fit are penalized. The stellar rotation period is finally calculated as the inverse of the frequency having the highest power.

4.4.3 Sine-fitting of stars with long periods

The techniques described in Sects. 4.4.1 and 4.4.2 are limited to periods shorter than the duration of the K2 campaigns (33 d for C0 and 70...80 d for the other campaigns). However, by visual inspection of the lightcurves we identify 11 stars with clearly sine-like variations that exceed the K2 monitoring time baseline. For these objects a least-squares fit allows us to constrain the rotation periods. The fitting was done with the routine CURVE_FIT in the Python package SciPy (Jones et al. 2001–) As initial guesses for the parameters we used four times the standard deviation as amplitude, a period of 30 d, and a phase of 0.0, but the results do not depend on this choice. For all 11 lightcurves the routine converges on a unique solution independent of the choice of the initial guesses for the parameters. In three cases the sinecurve provides only a crude approximation because the lightcurve is not symmetric around maximum or minimum and shows signs of spot evolution; in these cases the results are treated with caution.

4.4.4 Comparison of results from different period search algorithms

The results of the different period search methods are compared in Fig. 8. Generally, the LS and the ACF periods are in excellent agreement. For further use, based on the agreement between the periods obtained with the two techniques and considering the appearance of the phase folded lightcurve, we adopt either the ACF or the LS period as rotation period. This selection is made independently by two members of the team (BS and AS), and the results deviate for only few stars. For those dubious cases we make use of the SIP results as cross-check, and we adopt the period (either LS or ACF) which is in better agreement with the SIP "S/N" period. In addition, for the 11 stars that have their highest peak in the ACF and LS at a period corresponding to the length of the data set ($T_{\rm tot}$) but for which visual inspection reveals a clear (sine-like) pattern indicating a spot-modulation with $P_{\rm rot} > T_{\rm tot}$ we use the periods from the sine-fitting. From a comparison of the values obtained with the ACF and with the LS periodogram we estimate the typical error on our periods to be $\lesssim 3$ %. The final, adopted periods are given in Table 2 together with a quality flag and reference to the method with which it was derived. Flag 'Y' stands for reliable periods, '?' for questionable period detections, and 'N' for no period. These periods are obtained from the 'cleaned' lightcurves, but they are not significantly different from the periods found on the original, detrended lightcurves.

[7] We downloaded the Kepler lightcurves from the Target Search page at https://archive.stsci.edu/kepler/kepler_fov/search.php

[8] K2 raw and 'eigen' light curves were downloaded from http://bbq.dfm.io/ketu/lightcurves/ and http://bbq.dfm.io/ketu/elcs/

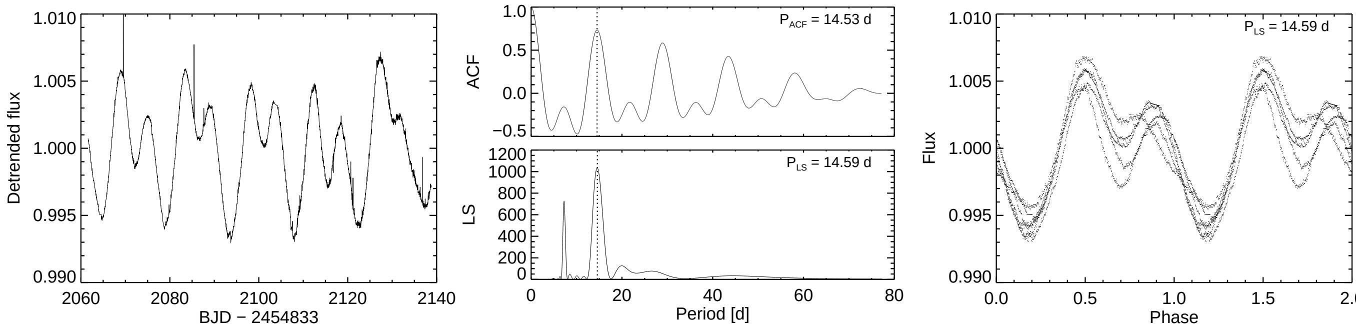

Figure 7. Example of detrended K2 lightcurve (left panel), ACF and LS periodogram (middle panel), and lightcurve folded with the ACF period (right panel).

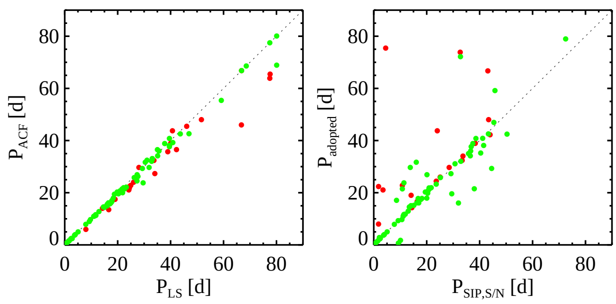

Figure 8. Comparison of the periods derived with the different methods described in Sect. 4.4. Reliable periods (green; flag 'y' in Table 2), questionable periods (red; flag '?').

Table 2. Rotation and activity parameters derived from the K2 lightcurves. The full table is available in the electronic version of the journal.

EPIC ID	$P_{\rm rot}$ [d]	method	flag	R_0	$R_{\rm per}$ [%]	$S_{\rm ph}$ [ppm]
202059188	0.69	LS	Y	0.01	2.754	10520.9
202059192	35.22	SINE	Y	0.78	0.559	1844.1
202059193	19.01	LS	?	0.42	0.469	1161.4
202059195	42.46	SINE	Y	0.63	1.814	6447.7
202059198	27.31	LS	Y	0.61	0.883	2802.3
202059199	...	—	N	-1.91	0.877	2508.0
202059203	...	—	N	-1.61	0.273	635.6
202059204	7.89	ACF	Y	0.18	2.760	8494.3

5 X-RAY EMISSION

We perform a systematic archive search for X-ray observations of the K2 Superblink M stars. Specifically, we consult the *XMM-Newton* Serendipitous Source Catalogue (3XMM-DR5; Rosen et al. 2015, A&A subm.[9]), the *XMM-Newton* Slew Survey Source Catalogue (XMMSL1_Delta6; Saxton et al. 2008), the Second *ROSAT* Source Catalog of Pointed Observations (2RXP) and the *ROSAT* Bright and Faint Source catalogs (BSC and FSC). Our procedure for cross-matching the K2 targets with these catalogs and for deriving X-ray fluxes and luminosities follow those described by Stelzer et al. (2013). We briefly summarize the individual steps here.

First, in order to ensure that no matches are missed due to the high proper motion of the most nearby stars (stars at < 10 pc have proper motions of $\sim 1''$/yr), the cross-correlation between the K2 target list and the X-ray catalogs is done after correcting the object coordinates from the K2 catalog[10] to the date of the X-ray observation using the proper motions given by LG11. We then use the following match radii between the X-ray catalog positions and the K2 coordinates: $40''$ for RASS (Neuhäuser et al. 1995), $30''$ for XMMSL (Saxton et al. 2008), $25''$ for 2 RXP (Pfeffermann et al. 2003) and $10''$ for 3XMM-DR5). With one exception all counterparts have much smaller separations than the respective cross-correlation radius (see Table 3). The only doubtful X-ray counterpart is the XMMSL source associated with EPIC 201917390. It has a separation close to the edge of our match circle which – as stated by Saxton et al. (2008) – is a generous interpretation of the astrometric uncertainty of the XMMSL. Since the same star is also clearly identified with a RASS source at an X-ray luminosity within a factor of two of the XMMSL source, we decide to keep the XMMSL counterpart. For all but one of the X-ray detected stars the rotation period could be determined. The exception is EPIC 210500368 for which hints for pseudo-periodic variations in the K2 lightcurve can be seen by-eye but the ACF and LS periodograms show no dominant peak.

After the identification of the X-ray counterparts we compute their $0.2-2$ keV flux assuming a 0.3 keV thermal emission subject to an absorbing column of $N_{\rm H} = 10^{19}\,{\rm cm^{-2}}$. The *ROSAT* count-to-flux conversion factor is determined with PIMMS[11] to be $CF_{\rm ROSAT} = 2.03 \cdot 10^{11}\,{\rm cts\,erg^{-1}\,cm^{-2}}$ (see also Stelzer et al. 2013) and we apply it to the count rates given in the 2 RXP catalog, the BSC and the FSC. For 3XMM-DR5 sources we use the tabulated EPIC/pn count rates in bands $1-3$ which represent energies of $0.2-0.5$, $0.5-1.0$, and $1.0-2.0$ keV, respectively. We sum the count rates in these bands, and perform the flux conversion for the combined $0.2-2.0$ keV band. All 3XMM-DR5 counterparts to K2 Superblink M stars were observed with the EPIC/pn medium filter, and for the $N_{\rm H}$ and kT given above we find in PIMMS a count-to-flux conversion factor of $CF_{\rm 3XMM-DR5} = 9.22 \cdot 10^{11}\,{\rm cts\,erg^{-1}\,cm^{-2}}$. The XMMSL1 catalog has the three energy bands already combined in columns 'B5'.

A total of 26 K2 Superblink stars have an X-ray counterpart in the archival databases that we have consulted. The X-ray fluxes

[9] http://xmmssc.irap.omp.eu/3XMM_v10.pdf

[10] Note, that the coordinates provided in the target lists of the individual K2 campaigns at http://keplerscience.arc.nasa.gov/k2-approved-programs.html refer to epoch 2000, except for campaign C0 where the coordinates seem to refer to the date of observation (Mar - May 2014).

[11] The Portable Interactive Multi-Mission Simulator is accessible at http://cxc.harvard.edu/toolkit/pimms.jsp

Table 3. X-ray parameters derived from archival data. For stars with multiple detections the mean X-ray luminosity is given. $\mathrm{Sep}_{\mathrm{x,opt}}$ are the separations between X-ray and K2-EPIC position.

EPIC ID	$\log L_{\mathrm{x}}$ [erg/s]	$\mathrm{Sep}_{\mathrm{x,opt}}$ [$''$]	Ref.cat
202059204	28.6	5.2	BSC
202059229	29.2	3.6	BSC
202059231	28.2	13.4	FSC
201482319	28.2	7.6, 14.0	BSC, 2RXP
201518346	26.8	7.2, 10.8	2RXP, BSC
201675315	27.1	1.4	3XMM
201806997	29.4	6.8	BSC
201917390	28.5	8.4, 29.1	BSC, XMMSL
201842163	28.5	22.8	BSC
201909533	28.8	2.8	BSC
202571062	29.5	13.0, 5.6	XMMSL, XMMSL
204927969	28.1	2.3	BSC
204957517	27.8	1.0	2RXP
205467732	27.4	8.9	FSC
205913009	26.1	0.6	3XMM
206019392	26.2	0.3, 9.0	3XMM, 2RXP
206208968	28.8	18.3	BSC
206262336	28.6	13.4	BSC
206349327	28.7	2.2	BSC
210434976	28.4	26.3	BSC
210500368	27.9	0.8	3XMM
210613397	29.4	11.0	BSC
210651981	28.7	8.2, 12.5	XMMSL, BSC
210707811	28.3	18.3	FSC
210741091	28.7	6.0, 10.7	2RXP, 2RXP
211111803	28.7	17.8	FSC

obtained as described above are converted to luminosities using the updated photometric distances of the stars (see Sect, 3). They are given in Table 3 together with the separation between X-ray and optical position and the respective X-ray catalog. For stars with more than one epoch of X-ray detection the luminosities are in agreement within a factor of two and we provide the mean of the two values.

6 ULTRAVIOLET EMISSION

To assess the UV activity of the K2 Superblink stars we cross-match our target list with the *GALEX-DR5 sources from AIS and MIS* (Bianchi et al. 2012). GALEX performed imaging in two UV bands, far-UV (henceforth FUV; $\lambda_{\mathrm{eff}} = 1528\,\mathrm{\AA}$, $\Delta\lambda = 1344 - 1786\,\mathrm{\AA}$) and near-UV (henceforth NUV; $\lambda_{\mathrm{eff}} = 2271\,\mathrm{\AA}$, $\Delta\lambda = 1771 - 2831\,\mathrm{\AA}$). The All-Sky Survey (AIS) covered $\sim 85\,\%$ of the high Galactic latitude ($\|b\| > 20^{\circ}$) sky to $\mathrm{m}_{AB} \sim 21\,\mathrm{mag}$, and the Medium Imaging Survey (MIS) reached $\mathrm{m}_{AB} \sim 23\,\mathrm{mag}$ on 1000 deg^2 (e.g. Bianchi 2009).

Analogous to our analysis of the X-ray data, we correct the coordinates from the K2 catalog to the date of the respective UV observation. We use a match radius of $10''$, but none of the UV counterparts we identify is further than $3''$ from the proper motion corrected K2 position. The GALEX-DR5 catalog provides NUV and FUV magnitudes which we convert to flux densities using the zero points given by Morrissey et al. (2005).

We isolate the chromospheric contribution to the UV emission from the photospheric part with help of synthetic DUSTY spectra of Allard et al. (2001), following the procedure described by Stelzer et al. (2013). We adopt the model spectra with solar metallicity and $\log g = 4.5$, and we choose for each star that model from the grid which has T_{eff} closest to the observationally determined value derived in Sect. 3. We then obtain the predicted photospheric UV flux density $[(f_{\mathrm{UV_i,ph}})_{\lambda}]$ in the two GALEX bands ($i = NUV, FUV$) from the UV and J band flux densities of the DUSTY model (i.e. the synthetic $UV_i - J$ color) and the observed J band flux density. The model flux densities in the FUV, NUV and J bands are determined by convolving the synthetic spectrum with the respective normalized filter transmission curve. Finally, the FUV and NUV fluxes are obtained by multiplying $(f_{\mathrm{UV_i,ph}})_{\lambda}$ with the effective band width of the respective GALEX filter ($\delta\lambda_{\mathrm{FUV}} = 268\,\mathrm{\AA}$; $\delta\lambda_{\mathrm{NUV}} = 732\,\mathrm{\AA}$); Morrissey et al. (2007). The expected photospheric fluxes ($f_{\mathrm{UV_i,ph}}$) are then subtracted from the observed ones to yield the chromospheric fluxes. We refer to these values as 'UV excess', $f_{\mathrm{UV_i,exc}}$. Finally, we define the UV activity index as $R'_{UV_i} = \frac{f_{\mathrm{UV_i,exc}}}{f_{\mathrm{bol}}}$ where f_{bol} is the bolometric flux. The superscript ($'$) indicates, in the same manner as for the well-known Ca II H&K index, that the flux ratio has been corrected for the photospheric contribution.

We find NUV detections for 41 stars from the K2 Superblink M star sample, i.e. roughly $30\,\%$, while only 11 stars ($\sim 8\,\%$) are identified as FUV sources. Stelzer et al. (2013) have shown that the photospheric contribution to the FUV emission of M stars is negligible while the fraction of the NUV emission emitted by the photosphere can be significant. We confirm here for the K2 Superblink M stars with FUV detections that this emission is entirely emitted from the chromosphere, i.e. $f_{\mathrm{FUV,ph}}$ is orders of magnitude smaller than the observed FUV flux. The NUV emission of the K2 Superblink M stars is also only weakly affected by photospheric contributions with $f_{\mathrm{NUV,ph}}$ less than $\sim 10\,\%$ of the observed flux for all stars. In Table 4 we provide the observed FUV and NUV magnitudes and the calculated chromospheric excess, $L_{\mathrm{UV_i,exc}}$, of all detected objects.

7 RESULTS

7.1 Period statistics and comparison with the literature

We could determine reliable periods for 76 stars (flag 'Y' in Table 2), and periods with lower confidence are found for 22 stars (flag '?'). Twelve stars of our sample have a previously reported period based on the same K2 data in Armstrong et al. (2015). In all but two cases those periods agree within $1 - 2\,\%$ with our values. The exceptions are EPIC-202059204 for which the lightcurves used by us (and produced by A.Vanderburg) show no evidence for the 5.04 d period provided by Armstrong et al. (2015), and EPIC-201237257 for which our adopted period is twice the value of 16.2 d presented by Armstrong et al. (2015) based on the maximum peak in both our ACF and LS periodogram. Periods for a small number of K2 Superblink stars have been presented previously also in the following studies: Survey in the southern hemisphere using the All-Sky Automated Survey (ASAS; Kiraga 2012, 6 stars), HATnet survey in the Pleiades (Hartman et al. 2010, 2 stars), SuperWASP survey in the Hyades and Pleiades (Delorme et al. 2011, 1 star), and from the compilation of (Pizzolato et al. 2003, 1 star). They are all in excellent agreement with our values derived from the K2 lightcurves. For the two stars we have in common with the HATNet survey of field stars presented by Hartman et al. (2011), however, we find strongly discrepant values for the periods: 16.1 d vs 39.0 d in Hartman et al. (2011) for EPIC-211107998 and 12.9 d vs 0.86 d in Hartman et al. (2011) for EPIC-211111803. We see no

Table 4. UV parameters derived from archival GALEX data.

EPIC ID	NUV [mag]	FUV [mag]	$\log L^{\dagger}_{\rm NUV}$ [erg/s]	$\log L^{\dagger}_{\rm FUV}$ [erg/s]
201237257	19.95 ± 0.13		28.3	
201460770	21.89 ± 0.40		27.8	
201482319	20.17 ± 0.16	21.54 ± 0.48	27.6	26.9
201506253	21.20 ± 0.19		28.1	
201518346	21.16 ± 0.36		26.0	
201568682	21.07 ± 0.22		28.5	
201611969	21.85 ± 0.30		27.5	
201675315	20.95 ± 0.27		28.2	
201719818	19.14 ± 0.08	22.05 ± 0.47	28.5	27.3
201917390	20.20 ± 0.15	21.47 ± 0.38	27.9	27.3
201367065	21.41 ± 0.22		28.2	
201497866	21.28 ± 0.34		27.9	
201842163	20.02 ± 0.11	21.39 ± 0.29	28.2	27.6
201909533	18.45 ± 0.04	20.06 ± 0.12	28.6	27.9
204963027	19.86 ± 0.17		28.3	
204927969	20.18 ± 0.20		27.8	
204994054	20.70 ± 0.28		28.3	
206007536	19.99 ± 0.09		28.7	
206019392	20.07 ± 0.09	22.63 ± 0.42	26.4	25.3
206054454	21.44 ± 0.25	22.12 ± 0.46	27.8	27.4
206055065	19.87 ± 0.10		28.9	
206056832	21.45 ± 0.25		28.5	
206107346	19.02 ± 0.05	21.86 ± 0.30	28.2	27.0
206208968	18.89 ± 0.08	20.14 ± 0.21	28.2	27.6
206368165	22.54 ± 0.47		27.6	
206479389	21.57 ± 0.33		27.9	
206490189	21.96 ± 0.30		27.4	
210393283	21.57 ± 0.41		28.0	
210434976	20.18 ± 0.16		27.7	
210460280	20.76 ± 0.20		28.0	
210500368	21.80 ± 0.40		28.0	
210502828	20.49 ± 0.18		28.5	
210535241	21.75 ± 0.35		28.1	
210579749	19.58 ± 0.09	21.40 ± 0.40	27.9	27.1
210585703	21.97 ± 0.40		27.7	
210592074	20.33 ± 0.33		28.8	
210613397	19.69 ± 0.09	21.66 ± 0.39	28.8	27.9
210757663	21.65 ± 0.39		28.1	
210778181	20.30 ± 0.18		28.5	
211008819	18.81 ± 0.08		28.5	
211036776	21.08 ± 0.22		27.9	

† Chromospheric 'excess' luminosities after subtraction of the photospheric contribution

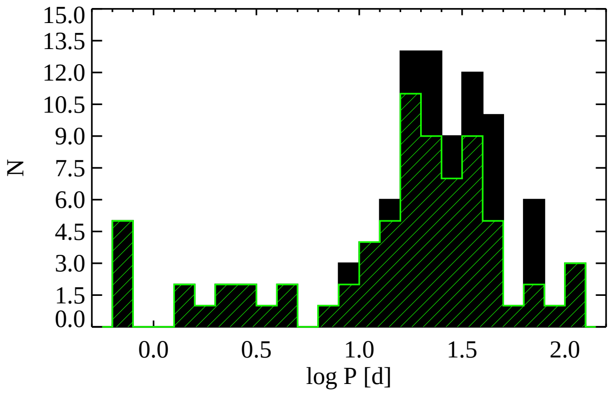

Figure 9. Distribution of the 98 rotation periods determined for the K2 Superblink M star sample. The black filled histogram represents the full sample of periods, and the overlaid green histogram the subsample of reliable periods (flag 'Y').

evidence in the K2 data for the period values determined by Hartman et al. (2011).

All in all, a 73 % of the K2 Superblink sample shows periodic variability on timescales up to $\sim$ 100 d. Our period distribution is shown in Fig. 9. Studies of rotation of M stars in the main Kepler mission have come up with 63 % (McQuillan et al. 2013) and 81 % (McQuillan et al. 2014) of stars with detected periods. These differences may reflect the different data sets (each K2 campaign provides a lightcurve corresponding to the length of about one quarter of Kepler data) and detection methods (we use sine-fitting in addition to ACF and periodograms). In particular, we establish here in a relatively unbiased sample of M dwarfs periods of $\sim$ 100 d and longer, in agreement with results from ground-based studies (Irwin et al. 2011; Newton et al. 2015). The period distribution of the Kepler sample from McQuillan et al. (2013) shows a cut at $\sim$ 65 d and McQuillan et al. (2014) explicitly limit their sample to periods $<$ 70 d. Note, that McQuillan et al. (2013) have performed the period search on individual Kepler Quarters which are of similar duration as the K2 campaigns. In fact, we are able to detect such long periods only thanks to the least-squares sine-fitting. We find that $\sim$ 10 % of the periods are longer than 70 d. These would not have been detected by the methods of McQuillan et al. (2013, 2014). An additional possible explanation for the absence of long-period variables in McQuillan et al. (2013) – related to photometric sensitivity – is presented in Sect. 7.3.

7.2 Rotation period and stellar mass

We present the newly derived rotation periods for the K2 Superblink M star sample in Fig. 10 as a function of stellar mass together with results for studies from the main Kepler mission. The sample of McQuillan et al. (2013) (black open circles) covered stars in the mass range of 0.3...0.55 $M_{\odot}$ selected based on the $T_{\rm eff}$ and $logg$ values from the Kepler input catalog (Brown et al. 2011). Subsequently, McQuillan et al. (2014) (black dots) extended this study with similar selection criteria to all stars with $T_{\rm eff} < 6500$ K. Among the most notable findings of these Kepler studies was a bimodal period distribution for the lowest masses, and an increasing upper envelope of the period distribution for decreasing mass. While we have too few objects to identify the bimodality, we confirm the upwards trend in the longest periods detected towards stars with lower mass. We are able to measure longer periods than McQuillan et al. (2013) and McQuillan et al. (2014) because we add sine-fitting to the ACF and periodgram period search methods; see Sect. 7.3 for a more detailed comparison of the period detection techniques and their implications. The fact that we measure periods in excess of $\sim$ 100 d only in stars with very low mass ($M \leqslant 0.45\,M_{\odot}$) is interesting. If it is a real feature in the rotational distribution, it suggests a change of the spin-down efficiency at the low-mass end of the stellar sequence. Note, however, that the stellar masses at which the upturn is seen to set in does not correspond to the fully convective transition ($\sim$ 0.35 $M_{\odot}$) where one might expect some kind of "mode change" in the dynamo. Also, we can not exclude that there are detection biases, e.g. the size and distribution of star spots and their lifetimes could be mass-dependent such that smaller and more quickly changing amplitudes are induced in higher-mass stars which would prevent us from detecting very long

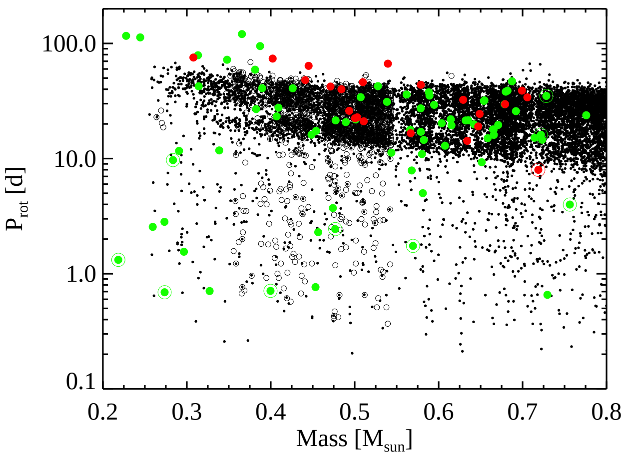

Figure 10. Period versus mass for the K2 Superblink M star sample (green and red symbols for periods flagged 'Y' and '?', respectively). Data from Kepler studies are plotted as open circles (McQuillan et al. 2013) and black dots (McQuillan et al. 2014). Binaries are marked with annuli (see Appendix).

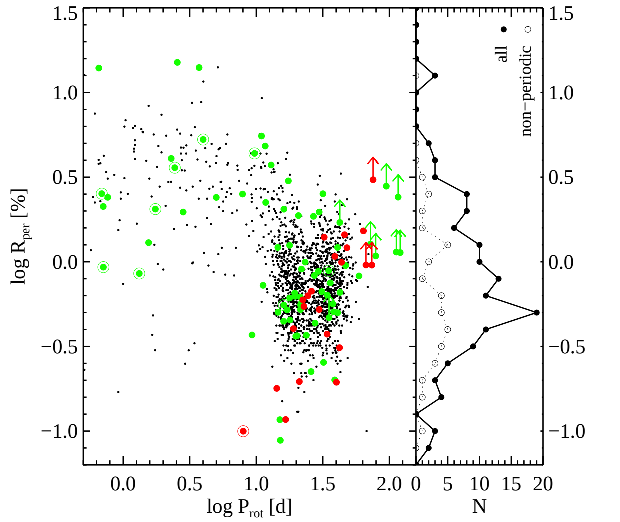

Figure 11. Period versus amplitude for the K2 Superblink M dwarf sample (large, colored circles) compared to the Kepler field M dwarfs from McQuillan et al. (2013) (small, black dots). For our K2 sample we distinguish reliable periods (green) and questionable periods (red). Banner on the right: histogram of $R_{\rm per}$ for the full K2 Superblink star sample (solid line) and for the subsample classified as non-periodic (flag 'N'). As in the other figures, binaries are marked with large annuli.

periods in them. A more detailed investigation of these features must be deferred to studies on a larger sample.

7.3 Activity diagnostics from K2 rotation cycles

We examine now various other diagnostics for rotation and activity derived from the K2 data. These are listed together with the rotation periods in Table 2.

The Rossby number (in col.5) is defined as $R_0 = P_{\rm rot}/\tau_{\rm conv}$, where $\tau_{\rm conv}$ is the convective turnover time obtained from $T_{\rm eff}$ using Eq. 36 of Cranmer & Saar (2011) and its extrapolation to $T_{\rm eff} < 3300$ K. There is no consensus on the appropriate convective turnover times for M dwarfs beyond the fully convective boundary. As pointed out by Cranmer & Saar (2011), the extrapolated values for late-M dwarfs ($\tau_{\rm conv} \sim 60...70$ d) are in reasonable agreement with semi-empirical values derived by Reiners et al. (2009) but significantly lower than the predictions of Barnes & Kim (2010). The Rossby number is a crucial indicator of dynamo efficiency and is used in Sect. 7.7 for the description of the rotation - activity relation. The parameters $R_{\rm per}$ (col.6) and $S_{\rm ph}$ (col.7) are measures for the variability in the K2 lightcurve and are examined in this section.

The lightcurve amplitude is determined by the contrast between spotted and unspotted photosphere and may, therefore, be considered a measure for magnetic activity. Various photometric activity indices characterizing the amplitude of Kepler lightcurves have been used in the literature. Basri et al. (2013) have introduced the range of variability between the 5th and 95th percentile of the observed flux values, $R_{\rm var}$. This definition is meant to remove the influence of flares which are occasional events involving only a small fraction of a given rotational cycle. To further reduce the influence of outliers, we follow the modified definition of McQuillan et al. (2013): $R_{\rm per}$ is the mean of the $R_{\rm var}$ values measured individually on all observed rotation cycles, expressed in percent.

Since in the course of our flare analysis we produce lightcurves where flares and other outliers have been eliminated we could use those "cleaned" lightcurves for the analysis of the rotational variability. This way we could avoid cutting the top and bottom 5 % of the data points. We compute the difference between the full amplitudes measured on the "cleaned" lightcurves and the $R_{\rm per}$ values measured on the original lightcurves and find them to differ by $\sim 0.05 \pm 0.05$ dex in logarithmic space. This is negligible to the observed range of amplitudes. In order to enable a direct comparison to results from the literature, we prefer, therefore, to stick to the $R_{\rm per}$ values derived from the original lightcurves. In Fig. 11 we show the relation between $P_{\rm rot}$ and $R_{\rm per}$ for the K2 Superblink M stars compared to the much larger Kepler M dwarf sample of McQuillan et al. (2013). The distribution of the two samples is in good agreement. In particular, stars with shorter periods have larger spot amplitudes. We examine this finding in more detail below.

Fig. 11 also illustrates the difference between our results and those of McQuillan et al. (2013) for the longest periods. [Note that all K2 Superblink stars with periods inferred from sine-fitting have only a lower limit to the variability amplitude $R_{\rm per}$.] One reason for the absence of long-period stars in McQuillan et al. (2013) could be the larger distance of the Kepler stars which results in lower sensitivity for small amplitudes, suggesting that Kepler can find periods only in the more active stars likely to be rotating faster. However, remarkably, the long-period stars in the K2 Superblink M star sample seem to have larger spot amplitudes than stars with lower periods (from $\sim$ 15...50 d). We recall again that we are able to detect such long periods only on stars with clear sine-like variation indicating the presence of a single dominating spot. Therefore, we can only speculate that stars with periods $\gtrsim$ 100 d and low spot amplitude may exist but their more diffuse spot patterns or changes on time-scales shorter than the rotation period yield a complex lightcurve. If so, one can expect these stars among the ones classified as non-periodic (flag 'N') by us. The bar on the right of Fig. 11 shows the distribution of $R_{\rm per}$ for all K2 Superblink M stars and for the subsample to which we could not assign a period. There is no clear preference of these latter ones towards small amplitudes, and the above consideration does not allow us to conclude on their periods. Constraining the range of spot amplitude of the slowest rotators should be a prime goal of future studies on larger samples. As described in Sect. 7.2 we find the longest periods exclusively in very low-mass stars. Therefore, the change in the distribution of the $R_{\rm per}$ values for the slowest rotators – if truly existing – might be a mass-dependent effect rather than related to rotation.

Mathur et al. (2014) defined the standard deviation of the full lightcurve, $S_{\rm ph}$, and $\langle S_{\rm ph,k} \rangle$, the mean of the standard deviations computed for time intervals $k \cdot P_{\rm rot}$. They found that for increasing k the index $\langle S_{\rm ph,k} \rangle$ approaches $S_{\rm ph}$. This way they were able to show that roughly after five rotation cycles ($k = 5$) the full range of flux variation is reached, and they recommend $\langle S_{\rm ph,k=5} \rangle$ as measure of the global evolution of the variability. We compute $S_{\rm ph}$ and $\langle S_{\rm ph,k=5} \rangle$ for the K2 Superblink M stars and show the results in Fig. 12 versus the rotation periods; filled circles represent $\langle S_{\rm ph,k=5} \rangle$ and open circles mark $S_{\rm ph}$. The sample studied by Mathur et al. (2014) is also displayed (black dots for their $\langle S_{\rm ph,k=5} \rangle$ values). That sample consists of 34 Kepler M stars with 15 Quarters of continuous observations and $P_{\rm rot} < 15$ d from the Kepler study of McQuillan et al. (2013). Our sample improves the period coverage especially for $P \lesssim 12$ d. The fact that there are no very fast rotators in the sample studied by Mathur et al. (2014) is probably a bias related to their sample selection. We find that stars with short periods have systematically larger $\langle S_{\rm ph,k=5} \rangle$ index than stars with $P \gtrsim 10$ d. The upper boundary of 15 d for the periods in the Mathur et al. (2014) sample is imposed by their requirement of covering at least 5 cycles. However, as explained above there is no dramatic difference between $\langle S_{\rm ph,k=5} \rangle$ and $S_{\rm ph}$ for a given star. We verify this on the K2 Superblink M star sample by showing as open circles their values $S_{\rm ph}$. The advantage of $S_{\rm ph}$ is that we can include in Fig. 12 the stars with $P > 1/5 \cdot \Delta t$. We can see that the pattern over the whole period range is very similar to that of Fig. 11, i.e. both spot amplitude and standard deviation of the lightcurve show a dependence on rotation rate which seems to divide the stars in two groups above and below $P \sim 10...12$ d.

7.4 Activity diagnostics related to flares in K2 lightcurves

Our separate analysis of flares and rotation in the K2 lightcurves enables us to relate flare activity to star spot activity. Fig. 13 shows the peak amplitudes of all flares defined with respect to the flattened K2 lightcurve (top panel) and the flare frequency of all stars (bottom panel) as function of the rotation period. A clear transition takes place near $P_{\rm rot} \sim 10$ d, analogous to the case of the spot activity measures discussed in Sect. 7.3. While the absence of small flares in fast rotators is determined by the noise level in the flattened lightcurve (see Fig. 6), there is no bias against the detection of large flares in slowly rotating stars. Note that our algorithm has lower flare detection sensitivity for events on fast-rotating stars because the presence of flares itself impacts on the quality of the smoothing process used to identify the flares. Therefore, especially for the stars with short periods, the number of flares observed per day ($N_{\rm flares}$/day) may represent a lower limit to the actual flare frequency.

7.5 Residual activity in K2 lightcurves

Above we have shown that both the spot cycle amplitude and the flares display a distinct behavior with rotation period. Here we examine the standard deviation of the "flattened" lightcurves, $S_{\rm flat}$.

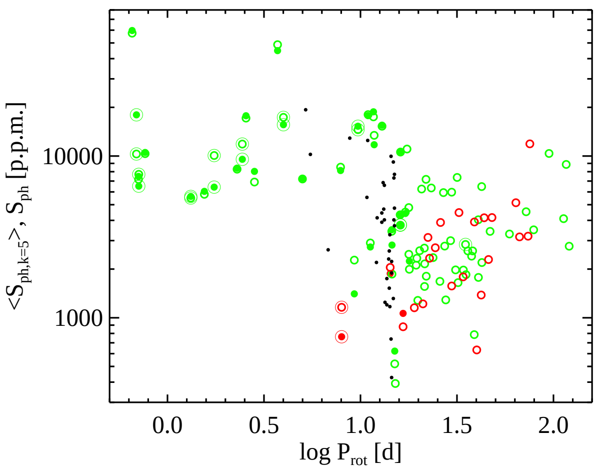

Figure 12. Magnetic activity indices defined by Mathur et al. (2014) vs period for the K2 Superblink star sample, compared to the subsample of 34 Kepler field M dwarfs studied by Mathur et al. (2014) (black dots). Green and red symbols represent periods flagged 'Y' and '?', respectively. Filled circles denote $\langle S_{\rm ph,k=5} \rangle$ values and open circles the $S_{\rm ph}$ values. See text in Sect. 7.3 for details on the definition of these indices. Large annuli mark binaries.

As described in Sect. 4.2, when measured without considering the outliers, this parameter represents a measure for the noise after removal of the rotation cycle and of the flares. We notice a marked trend of $S_{\rm flat}$ with the rotation period (Fig. 14). A dependence of the noise level on the brightness of the star is expected and demonstrated in Fig. 6, where the lower envelope of the distribution increases towards fainter $K_{\rm p}$ magnitude. However, the difference between the $S_{\rm flat}$ values seen for slow and fast rotators in Fig. 14 is clearly unrelated to this effect. The evidently bimodal distribution with rapid rotators showing larger values of $S_{\rm flat}$, therefore suggests that there is a contribution to the 'noise' in the K2 photometry that is astrophysical in origin.

The similarity of the period dependence seen in $S_{\rm flat}$ (Fig. 14), the spot cycle (Fig. 11 and 12) and the flares (Fig. 13) may indicate that the 'noise' in the fastest rotators could be caused by unresolved spot or flare activity. Many small flares, so-called nano-flares, as well as many small and/or rapidly evolving spots can produce a seemingly stochastic signal. This astrophysical noise sources seem to be limited to fast rotators, while for slow rotators the spot contrast drops below a constant minimum level of the variability which might be identified as the photometric precision (see Sect. 4.3).

7.6 Photometric activity and binarity

In the relations between various activity indicators and rotation period presented in the previous sections, binary stars that have a possible contribution to the rotational signal from the unresolved companion star are highlighted. Strikingly, the binaries are mostly associated with rotation periods below the transition between fast and slow regimes that we have identified. In Fig. 14 this could be taken as evidence that the presence of a companion increases the noise in the K2 lightcurve. On the other hand, we have argued above that the coincidence of the bimodality in $S_{\rm flat}$, spot and flare signatures with $P_{\rm rot}$ points at a fundamental transition taking place in these stars. We may speculate that binarity is responsible for the observed

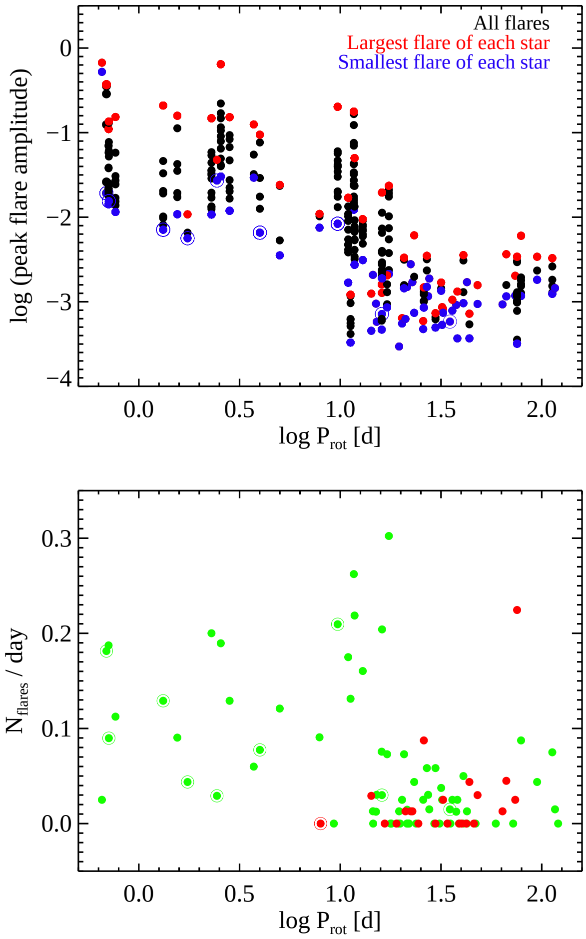

Figure 13. *top* - Flare amplitude vs rotation period: All flares are shown and the range of flare amplitudes for a given star is made evident by marking the largest and smallest flare on each star with different colors, red and blue respectively. *bottom* - Flare frequency vs rotation period: Each star is represented once. Binaries are highlighted in both panels with annuli.

dichotomy, e.g. by spinning up the star through tidal interaction or by reducing angular momentum loss. The binary fraction (BF) for the fast rotators ($P_{\rm rot} < 10$ d) is $8/19$, i.e. 8 stars out of 19 are known binaries. For slow rotators ($P_{\rm rot} > 10$ d) the binary fraction is $2/78$. We calculate the 95 % confidence levels for a binomial distribution and find the two samples to be significantly different: $BF_{\rm fast} = 0.42^{+0.67}_{-0.20}$ and $BF_{\rm slow} = 0.03^{+0.09}_{-0.00}$. That said, we caution that no systematic and homogeneous search for multiplicity was done for these stars and our literature compilation (Sect. A) may be incomplete.

7.7 The X-ray and UV activity – rotation relation

The activity – rotation relation is traditionally expressed using X-rays, Ca II H&K and Hα emission as activity indicators. Measurements of these diagnostics have historically been easiest to achieve (Pallavicini et al. 1981; Noyes et al. 1984). Yet, as described in Sect. 1, the dependence between magnetic activity and rotation has remained poorly constrained for M stars. In Fig. 15 we present an updated view using the X-ray data extracted from the archives and the newly derived rotation periods from K2. We also add here, to

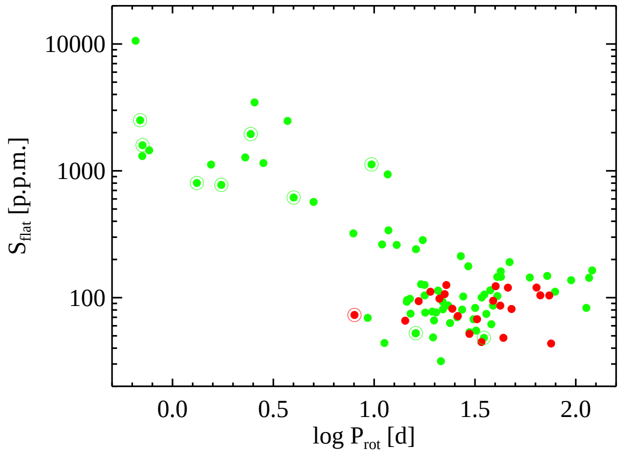

Figure 14. Standard deviation of the flattened lightcurve excluding the outliers, as in Fig. 6 but for all campaigns (C0...C4) and shown here vs rotation period. Green symbols (period flag 'Y'), red symbols (period flag '?'). The clear transition between fast and slowly rotating stars indicates that for fast rotators the origin of this 'noise' has an astrophysical component. Binaries are highlighted with annuli.

our knowledge for the first time for field M stars, UV emission as diagnostic of chromospheric activity.

All but two of the 26 K2 Superblink stars with X-ray detection have reliable rotation period measurement (flag 'Y'). The first exception is EPIC-206019392 for which we find through sine-fitting a period of $\sim$ 75 d. While there are no doubts on a periodic spot-modulation, the slight deviations of its lightcurve from a sinusoidal make the value for the period uncertain (therefore flagged '?' in Table 2). For the other case, EPIC-210500368, we can not identify a dominating period, yet the lightcurve shows a long-term trend superposed on a variability with a time-scale of $\sim$ 10 d. Among the NUV detections we could establish the rotation period for 78 % ($32/41$), and 46 % ($19/41$) of them have a 'reliable' period. Nine of 11 FUV detected stars have a period measurement, of which 7 are flagged 'reliable'.

The parameters which best describe the connection between activity and rotation are still a matter of debate (Reiners et al. 2014). We provide here plots for luminosity versus rotation period (left panels of Fig. 15) and for activity index $L_{\rm i}/L_{\rm bol}$ with $i = NUV, FUV, X$ versus Rossby number (right panels). First, it is clear that there is a decrease of the activity levels in all three diagnostics (NUV, FUV, X-rays) for the slowest rotators. While the sample of M stars with FUV detection and rotation period measurement is still very small, a division in a saturated and a correlated regime, historically termed the "linear" regime, can be seen in the relations involving NUV and X-ray emission. The X-ray – rotation relation is still poorly populated for slow rotators, and the turn-over point and the slope of the decaying part of the relation can not be well constrained with the current sample. Interestingly, for the NUV emission the situation is reversed, in a sense that more stars with NUV detection are found among slow rotators. In terms of luminosity NUV saturation seems to hold up to periods of $\sim$ 40 d, way beyond the critical period of $\sim$ 10 d identified to represent a transition in the behavior of optical activity indicators extracted from the K2 lightcurves (see Sect. 7.3 and 7.4). On the other hand, the $L'_{\rm NUV}/L_{\rm bol}$ values are slightly decreased with respect to the levels of the fastest rotators, and the active stars around

Table 5. X-ray saturation level for M dwarfs determined for X-ray detected stars with $P_{\rm rot} < 10\,{\rm d}$.

SpT	N_*	$\log L_{\rm x,sat}$ [erg/s]	$\log{(L_{\rm x,sat}/L_{\rm bol})}$
K7...M2	5	29.2 ± 0.4	-3.0 ± 0.4
M3...M4	8	28.6 ± 0.2	-3.2 ± 0.2
M5...M6	3	27.9 ± 0.5	-3.5 ± 0.5

a $\sim 30...40$ d period are all late-K to early-M stars. We also caution that a large fraction of the slowly rotating NUV detected stars have periods that we flagged as less reliable (red symbols in Fig. 15).

In order to highlight eventual differences emerging at the fully convective transition, we divide the stars in Fig. 15 into three spectral type groups represented by different plotting symbols. As far as the X-ray emission is concerned, the two order of magnitude scatter in the saturated part of the $L_{\rm x}$ vs $P_{\rm rot}$ relation is clearly determined by the spectral type distribution, with cooler stars having lower X-ray luminosities for given period. This is a consequence of the mass dependence of X-ray luminosity, and was already seen by Pizzolato et al. (2003) for coarser bins of stellar mass representing a spectral type range from G to M. We have overplotted in the bottom panels of Fig. 15 the relation derived by Pizzolato et al. (2003) for their lowest mass bin, $M = 0.22...0.60\,M_\odot$ (corresponding to spectral type earlier than M2). It must be noted that in Pizzolato et al. (2003) the linear regime was populated by only two stars of their sample and the saturated regime was dominated by upper limits to $P_{\rm rot}$ which were estimated from $v \sin i$ measurements. Therefore, even our still limited K2 sample constitutes a significant step forward in constraining the X-ray – rotation relation of M dwarfs.

We determine the saturation level for all X-ray detections with $P_{\rm rot} < 10\,{\rm d}$ in the three spectral type bins K7...M2, M3...M4, and M5...M6. The results are summarized in Table 5. If we select the K2 Superblink M star subsample in the same mass range studied by Pizzolato et al. (2003) ($M = 0.22...0.60\,M_\odot$) we derive saturation levels of $\log L_{\rm x,sat}\,[{\rm erg/s}] = 28.5 \pm 0.5$ and $\log{(L_{\rm x,sat}/L_{\rm bol})} = -3.3 \pm 0.4$, within the uncertainties compatible with their results. We confirm results of previous studies that the saturation level converges to a much narrower distribution if $\log{(L_{\rm x}/L_{\rm bol})}$ is used as activity diagnostic. However, albeit not yet statistically sound, the very low mass stars (SpT M5...M6) seem to be underluminous with respect to this level. It has been widely acknowledged that the activity levels show a drop for late-M dwarfs (e.g. West et al. 2008; Reiners et al. 2012), but an investigation of whether and how this is related to $P_{\rm rot}$ has come into reach only now with the large number of periods that can be obtained from planet transit search projects. Using rotation periods from the MEarth program, West et al. (2015) showed that the average $L_{{\rm H}\alpha}/L_{\rm bol}$ ratio for fast rotators ($P_{\rm rot} < 10...20\,{\rm d}$) decreases by a factor two for late-M dwarfs (SpT M5...M8) compared to early-M dwarfs (SpT M1-M4). Whether a distinct regime exists in which Hα activity correlates with $P_{\rm rot}$ could not be established in that study. The X-ray and UV detections we present in this paper also do not adequately sample the regime of long periods. We refrain here from fitting that part of the rotation-activity relation because our upcoming *Chandra* observations together with the larger sample of periods that will be available for Superblink M stars at the end of the K2 mission will put us in a much better position to address this issue.

7.8 Activity and rotation of planet host stars

Being bright and nearby, the K2 Superblink stars have special importance for planet search studies. In fact, at the time of writing of this paper two of our targets already have confirmed planets discovered by the K2 mission. K2-3 is a system comprising three super-Earths confirmed through radial velocity monitoring, with the outer planet orbiting close to the inner edge of the habitable zone (EPIC-201367065 observed in campaign C 1); see Crossfield et al. (2015); Almenara et al. (2015). K2-18 (EPIC-201912552, also observed in C 1) has a $\sim 2\,R_\oplus$ planet which was estimated to receive 94 ± 21 % of the Earth's insolation (Montet et al. 2015). Both host stars are prime targets for characterization studies of the planetary atmospheres through transit spectroscopy. Thus, the analysis of their stellar activity is a necessary step toward a global physical description of these systems.

Another two stars from our K2 Superblink sample have planet candidates presented by Vanderburg et al. (2016). These objects are not yet verified by radial velocity measurements. Our analysis shows that for both systems the stellar rotation is not synchronized with the planet orbital period ($P_{\rm orb} = 1.8\,{\rm d}$ for EPIC-203099398 and 14.6 d for EPIC-205489894, respectively).

8 DISCUSSION

We present here the first full flare and rotation period analysis for a statistical sample of K2 lightcurves. Our target list of bright and nearby M dwarfs represents a benchmark sample for exoplanet studies and will be thoroughly characterized by Gaia in the near future. Knowledge of the magnetic activity of these stars is of paramount importance given the potential impact it has on exoplanets. At the moment a planet is detected, the high-energy emission of any given K2 target and its variability becomes a prime interest (see e.g. Schlieder et al. 2016, for a recent example). With the study presented here and future analogous work on the remaining K2 campaigns we anticipate such concerns.

Our primary aim here is to understand the stellar dynamo and angular momentum evolution at the low-mass end of the stellar sequence through a study of relations between magnetic activity and rotation. We characterize activity with a multi-wavelength approach involving archival X-ray and UV observations as well as parameters extracted directly from the K2 lightcurves which describe spot amplitudes and flares. This way we provide a stratified picture of magnetic activity from the corona over the chromosphere down to the photosphere. To our knowledge this is the first time that the link with photometrically determined rotation periods is made for a well-defined sample of M stars over such a broad range of activity diagnostics.

Visual inspection of the K2 lightcurves shows that there is not a single non-variable star in this sample of 134 M dwarfs. We can constrain rotation periods in 73 % of them. The distribution of rotation periods we find for our sample is in general agreement with studies from the main Kepler mission with much larger but less well-characterized M star samples (McQuillan et al. 2013, 2014). Contrary to these studies we find long periods up to ~ 100 d, thanks to our complementary use of direct sine-fitting as period detection method next to ACF and LS periodograms. We detect such long periods only in the lowest mass stars ($M \leqslant 0.4\,M_\odot$). In this respect, our results resemble those obtained by Irwin et al. (2011); Newton et al. (2015) based on the MEarth program where sine-fitting yielded many long periods. However, unlike that project our sample includes also early-M type stars and, therefore, it has allowed

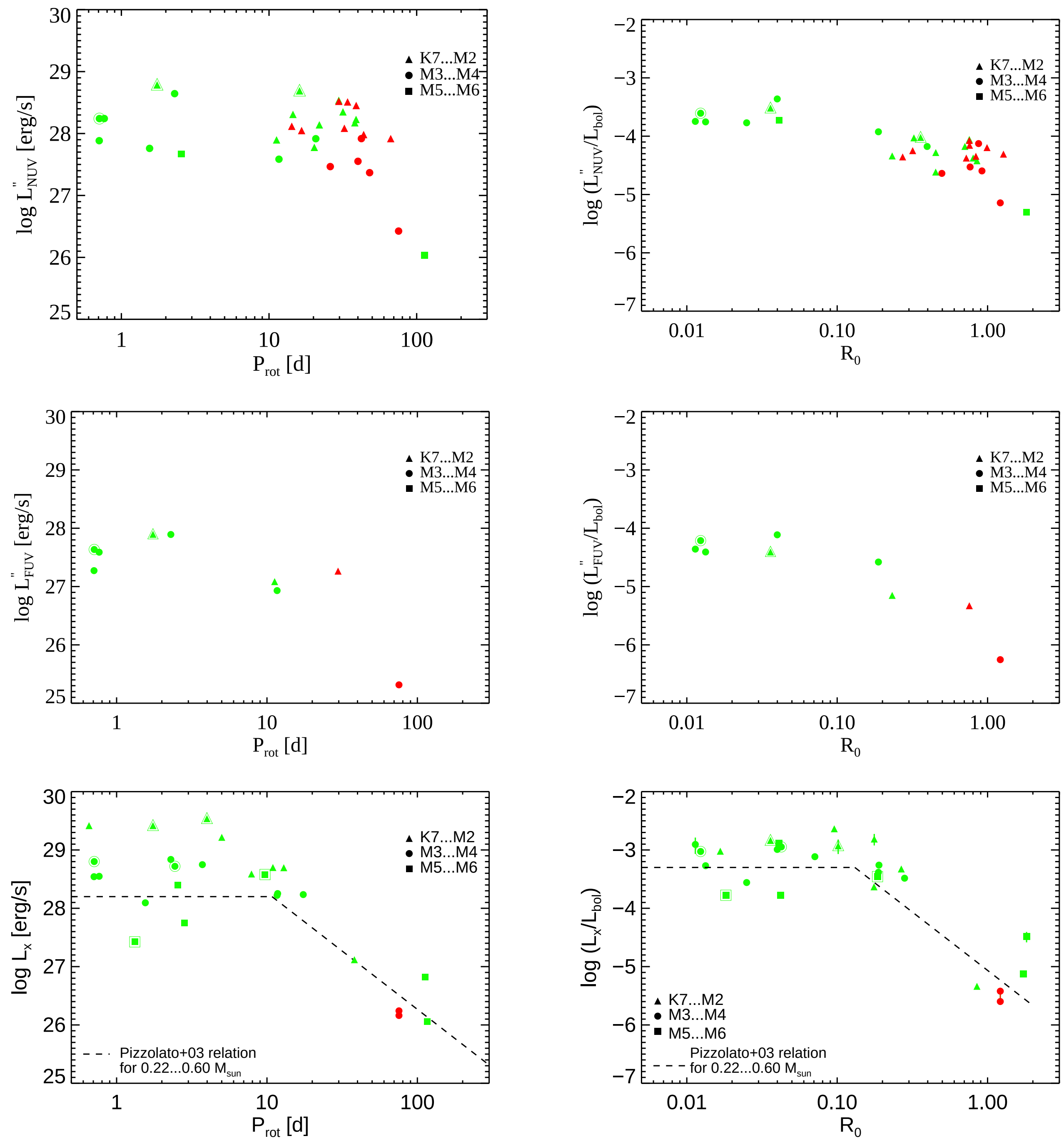

Figure 15. K2 rotation periods combined with archival NUV (top), FUV (middle) and X-ray (bottom) data for the campaign C0...C4 Superblink M stars. In the left panels, luminosities vs rotation period, in the right panels activity indices vs Rossby number. Periods flagged '?' are shown in red, unresolved binaries are represented with large annuli.

us to establish that there is a dearth of long periods in early-M dwarfs. Until corroborated by a larger sample, we can only speculate whether this is due to the evolution of spin-down history across the stellar mass sequence or whether it results from a change in spot pattern and related changes in the detection capabilities for the associated periods.

The low cadence of the K2 lightcurves allows us to detect only the flares with duration $\geqslant 1$ h, and due to this sparse sampling we refrain from a detailed analysis of flare statistics. Yet, we find an unprecedented link between flares and stellar rotation. The distribution of flare amplitudes and flare frequencies shows a clear transition at $P_{\rm rot} \sim 10$ d. The large flares seen in stars rotating faster than this boundary are absent in slow rotators although there is no detection bias against them. The smaller flares on slow rotators have no counterparts in the fast rotators but such events – if present – would likely be undetectable. We find the same bimodality between fast and slow rotators in the noise level ($S_{\rm flat}$) of the residual lightcurves after the rotational signal, flares and other 'outliers' are subtracted off: The residual variability seen in the fast rotators is significantly and systematically larger than in the slow rotators with a dividing line at $P_{\rm rot} \sim 10$ d. These new findings can now be added to the rotation-dependence of the spot cycle amplitude ($R_{\rm per}$) already known from the above-mentioned Kepler studies: A cut exists at the same period of ~ 10 d with faster rotating stars showing larger amplitudes of the rotation cycle. These similarities lead us to speculate that the 'noise' (i.e. the high values of $S_{\rm flat}$) seen in the fast rotators is produced by smaller or fast-changing spots or by microflares that cause seemingly random variations.

The observed dichotomy in photometric activity levels between fast and slow rotators points to a rotation-dependent rapid transition in the magnetic properties of the photospheres in M dwarfs. In fact, an analogous sharp transition is observed in some numerical dynamo models at $R_{0,l} \sim 0.1$, where $R_{0,l}$ is the 'local Rossby number' (e.g. Schrinner et al. 2012). Assuming this theoretical Rossby number corresponds with its empirical definition (see Sect. 7.3), this corresponds roughly to our observed critical period of ~ 10 d. In the simulations, for $R_{0,l} > 0.1$ (slow rotators) the dipolar component of the dynamo collapses giving way to a multipolar dynamo regime. Gastine et al. (2013) have compared these predictions to the magnetic field structure inferred from Zeeman Doppler Imaging of M dwarfs. Such observations are intricate and the samples tend to be biased towards fast rotators. When interpreted in terms of the above-mentioned models, our results suggest photometric rotation and activity measures as a new window for observational studies of dynamo flavors in M dwarfs. However, it must be questioned whether these diagnostics, which represent activity on the stellar surface, are sensitive to the large-scale component of the magnetic field.

The transition seen in star spots and white-light flares also corresponds approximately to the period where previous studies of the X-ray - rotation relation have placed the transition from the 'saturated' to the 'linear' regime (e.g. Pizzolato et al. 2003). Different explanations have been put forth for this finding involving the filling factor for active regions, the size of coronal loops or the dynamo mechanism. Observationally, those studies have so far shown clear rotation-activity trends only for higher-mass stars. We extend the X-ray – rotation relation here to well-studied M stars. We can refine our knowledge of X-ray emission in the saturated regime (fast rotation) in bins spanning two spectral subclasses and we find a continuous decrease of the saturation level $L_{\rm x}$ towards later spectral type which can be understood in terms of the mass dependence of X-ray luminosity. There is tentative evidence that the saturated stars in the coolest mass bin (spectral types M5...M6) may deviate from this behavior of constant $L_{\rm x}/L_{\rm bol}$ irrespective of spectral type seen for the K7...M4 type stars. If confirmed on a larger sample this might represent a change at the fully convective transition, whether due to magnetic field strength or structure, or its coupling to rotation (i.e. the stellar dynamo). It is by now well established that there is a sharp drop of X-ray and Hα activity at late-M spectral types ($\sim$ M7...M8; e.g. Cook et al. 2014; West et al. 2008) but for mid-M spectral types, so far, X-ray studies have not been resolved in both $P_{\rm rot}$ and spectral type space together. If, e.g., late-M stars remain saturated up to longer periods, the decrease of the saturation level may go unnoticed in samples mixing the whole rotational distribution.

We add in this study the first assessment of a link between rotation and chromospheric UV emission in M stars. Similar to the archival X-ray data, the UV data (from the GALEX mission) covers only a fraction of the K2 sample. A curious wealth of stars with high UV emission levels and long periods is seen that seems to be in contrast with the findings regarding all other activity indicators discussed in this work.

Finally, our archive search for evidence of multiplicity in our targets raises an interesting point about the possible influence of multiplicity on rotation and activity levels. We find a high incidence of binarity in the group of fast rotators below the critical period at which magnetic activity apparently transitions to a lower level. The difference between the binary fraction of fast and slow rotators is statistically significant. Given the rather large binary separations (of tens to hundreds of AU) this is puzzling because no tidal interaction is expected for such wide systems. Nevertheless, we can speculate about a possible causal connection between binarity and rotation level. It is well established that wide companions accelerate the evolution of pre-main sequence disks (e.g. Kraus et al. 2012). Shorter disk lifetimes translate into a shorter period of star-disk interaction and, hence, one may expect higher initial rotation rates on the main sequence for binary stars (Herbst & Mundt 2005). As a result, it may take binaries longer to spin down. Alternatively, we could be seeing the mass-dependence of magnetic braking. With our low-number statistics we can not draw any firm conclusions. Note, however, that a relation between fast rotation and binarity, independent of stellar mass, was also found in a recent K2 study of the Hyades (Douglas et al. 2016).

9 SUMMARY AND OUTLOOK

From a joint rotation and multi-wavelength activity and variability study of nearby M dwarfs observed in K2 campaigns C0 to C4 we infer a critical period of ~ 10 d at which photometric star spot and flare activity undergoes a dramatic change. This transition is coincident with the break seen in traditional studies of the rotation-activity relation probing higher atmospheric layers (e.g. the corona through X-rays or the chromosphere through Hα emission). We present here an updated view of the X-ray - rotation relation for M dwarfs. The sample analysed in this work has more than doubled the known number of long-period M dwarfs in the X-ray – rotation relation. Nevertheless, at present there is not enough sensitive data in the X-ray archives to constrain the X-ray – rotation relation for periods beyond ~ 10 d. A key questions is now whether the coronal emission of M dwarfs displays a break-point analogous to the optical photometric activity tracers or whether there is a continuous decrease of activity as seen in FGK stars. This problem will be addressed in the near future with upcoming *Chandra* observations in which we sample the whole observed K2 rotation period distribution. We will also further examine the UV – rotation relation in the larger M dwarf sample that will be available at the end of the K2 mission. Moreover, in that larger sample we intend to search for a possible mass dependence of the rotation-activity relation within the M spectral sequence. A systematic assessment of multiplicity for these nearby M stars with Gaia will also be useful for examining the influence of a companion star on rotation and activity levels.

The observed dichotomy between fast and slow rotators in terms of their magnetic activity level might have interesting consequences for habitability of planets near M stars being fried by flares and high-energy radiation until they have spun down to around 10 d. The time-scale for this process is as yet poorly constrained but certainly on the order of Gyrs, and it becomes longer the lower the mass of the star (West et al. 2008). Segura et al. (2010) found in models based on AD Leo that UV flares do not strongly affect planet chemistry but the accumulated effect of the exposure to strong flaring over most of the planet's lifetime has not been studied so far.

APPENDIX A: SEARCH FOR BINARITY

We search all K2 Superblink stars for archival evidence of binarity. We proceed in several steps. First, we perform a visual inspection of POSS1_RED and POSS2_RED photographic plates by using the online Digitized Sky Survey (DSS) and the interactive tools of Aladin. Epochs of each pair of plates are separated by up to ∼40 years, with the most recent plates obtained in the 1990s. Comparison of the two epochs can help in identifying possible blends in the K2 photometry. Specifically, we examine if the targets significantly approached other stars due to their proper motion. Then, we search for photometric and astrometric information of each possible contaminant by matching the UCAC4 and 2MASS catalogs in Vizier. Taking into account that the K2 pixel scale is $\sim 4''/\mathrm{pixel}$, for those cases with possible blends we check the K2 imagettes and the photometric mask produced and used by A.Vanderburg in the reduction of the K2 data [12] to estimate visually the occurrence of blending and its significance. For each target, the inspected imagette represents the sum of all the single imagettes recorded by K2 during a campaign. From our experience such merged imagettes are usually affected by the shift on the sensor of the photometric centroid due to pointing drift of the telescope. The photometric masks are wide enough to take into account the drift of the centroids, making any quantitative analysis of blending with other astrophysical objects rather difficult and beyond the scope of this work. We also search the Washington Double Star catalog (WDS) for information about binarity including sub-arcsec separations, which can not be detected simply by visual inspection of the photographic plates or matching with other catalogues. For binaries in the WDS we adopt the visual magnitude difference between the components indicated in the catalog, when available and other photometric measurements were missing.

With this approach, we find evidence for a companion for 25 stars. However, many of the secondaries have a J magnitude which is more than 4 mag fainter than our target. These secondaries contribute at most a few percent to the flux of the system. They are unlikely to be responsible for the observed rotational signal, and we do not consider them any further. We list the remaining potential companions in Table A1. These objects have either a J magnitude difference of < 4 mag with respect to the corresponding K2 target, or a small separation according to the WDS catalog without known photometry, or both. Next to an identifier for the putative companion (col.3) we provide the binary separation (col.4), the epoch to which it refers (col.5), the J magnitude or a magnitude difference between the two components according to the WDS (col.6-7), and flags indicating how we identfy it (through visual inspection of photographic plates, as entry in the WDS, or in the K2 imagette; cols.8-10). In a final 'Notes' column and in footnotes we add further explanations where needed.

The most important fact to note concerns the binary Gl 852 AB. Both stars are in our target list (EPIC-206262223 and EPIC-206262336) but they are clearly unresolved in A.Vanderburg's K2 pipeline. In fact, the lightcurves of both stars are identical because the aperture comprises an elongated object, clearly representing the two stars of the $8''$ binary. We also add a special note here on EPIC-204927969. Our inspection of the K2 imagette shows that the aperture used by Vanderburg includes other objects but our reconstruction of the lightcurve without the contaminated pixels proved that the rotational modulation is due to the target. Other possible contaminations to be taken serious regard the companions that have $J < 10$ mag. There are two such objects listed in Table A1. Another three K2 Superblink stars have companions with $J < 12.5$ mag which might contribute somewhat to the variability in the lightcurve. Further three multiples are presented in the literature, one spectroscopic binary and two close visual binaries. For the remaining objects in Table A1 we find no photometric measurements, and they are likely faint and may not influence the K2 lightcurves. All stars in Table A1 are flagged on the figures involving periods and activity measures from K2 data.

[12] https://www.cfa.harvard.edu/∼avanderb/k2.html

ACKNOWLEDGMENTS

We would especially like to thank A. Vanderburg for his public release of the analysed K2 lightcurves, upon which much of the present work is based. This research has made use of the VizieR catalogue access tool, and the "Aladin sky atlas", both developed at CDS, Strasbourg Observatory, France.

REFERENCES

Allard F., Hauschildt P. H., Alexander D. R., Tamanai A., Schweitzer A., 2001, ApJ, 556, 357
Almenara J. M. et al., 2015, A&A, 581, L7
Andersen J. M., Korhonen H., 2015, MNRAS, 448, 3053
Angus R., Foreman-Mackey D., Johnson J. A., 2015, ArXiv e-prints
Armstrong D. J. et al., 2015, A&A, 579, A19
Barnes S. A., Kim Y.-C., 2010, ApJ, 721, 675
Basri G., Walkowicz L. M., Reiners A., 2013, ApJ, 769, 37
Beuzit J.-L. et al., 2004, A&A, 425, 997
Bianchi L., 2009, Astrophys. Space Science, 320, 11
Bianchi L., Herald J., Efremova B., Girardi L., Zabot A., Marigo P., Conti A., Shiao B., 2012, VizieR Online Data Catalog, 2312
Borucki W. J. et al., 2010, Science, 327, 977
Bouvier J., Matt S. P., Mohanty S., Scholz A., Stassun K. G., Zanni C., 2014, Protostars and Planets VI, 433
Bowler B. P. et al., 2015, ApJ, 806, 62
Brown T. M., Latham D. W., Everett M. E., Esquerdo G. A., 2011, AJ, 142, 112
Browning M. K., Basri G., Marcy G. W., West A. A., Zhang J., 2010, AJ, 139, 504
Chabrier G., Küker M., 2006, A&A, 446, 1027
Cook B. A., Williams P. K. G., Berger E., 2014, ApJ, 785, 10
Cranmer S. R., Saar S. H., 2011, ApJ, 741, 54
Crossfield I. J. M. et al., 2015, ApJ, 804, 10
Davenport J. R. A. et al., 2014, ApJ, 797, 122
Delorme P., Collier Cameron A., Hebb L., Rostron J., Lister T. A., Norton A. J., Pollacco D., West R. G., 2011, MNRAS, 413, 2218
Donati J.-F., Landstreet J. D., 2009, ARA&A, 47, 333
Douglas S. T., Agüeros M. A., Covey K. R., Cargile P. A., Barclay T., Cody A., Howell S. B., Kopytova T., 2016, ArXiv e-prints
Durney B. R., De Young D. S., Roxburgh I. W., 1993, Sol.Phys, 145, 207

Table A1: Companions possibly contaminating the K2 photometry

EPIC ID	Campaign	Companion	Sep* [″]	Epoch	J [mag]	Δ [mag]	Evidence for binarity: Plates	WDS	K2	Notes
202059188	C0	WDS 06102+2234	1.90	2012	...		x	x		1954 vs 1997 plates: in 1997 the star was fully superposed with another object
201909533	C1	WDS 11519+0731	SB	2013	...	...		x		Triple star studied by Bowler et al. (2015); primary is a spectroscopic binary with nearly equal mass components; it forms a common proper motion pair with an object of spectral type M8V and $\Delta H = 5.4$ mag
202571062	C2	WDS 16240-2911	6.20	2009	9.60			x		Alternative name UCAC4 305-091749
203124214	C2	WDS 16254-2710	2.80	2000	...	0.5		x	x	Magnitude difference from WDS; no reference found
204976998	C2	UCAC4 351-084361	7.60	2000	11.25				x	
205467732	C2	WDS 16268-1724	0.50	2010	...	0.4		x		Magnitude difference from WDS; no reference found
205952383	C3	2MASS 22362748-16172	7.00	2000	12.24				x	
206007536	C3	UCAC4 377-172716	6.40	2000	10.71				x	
206208968	C3	WDS 22334-0937	1.50	2010	...	$0(J, K)$		x		Binary resolved by McCarthy et al. (2001) who report separation and magnitude difference
206262223†	C3	UCAC4 406-139520	8.00	2012	9.46				x	Companion of EPIC-206262336
	C3	WDS 22173-0847	0.70	2014	...	$1.2(K)$		x		Additional spectroscopic companion; separation and spectral type (M7V) from WDS; magnitude difference from Beuzit et al. (2004).
206262336†	C3	UCAC4 406-139522	8.00	2012	9.02				x	Companion of EPIC-206262223 (see above)
	C3	WDS 22173-0847	2.60	2010	...			x		Additional companion; separation from WDS
210613397	C4	WDS 03462+1710	14.3	2008	9.00			x	x	Alternative name UCAC4 536-007198. Companion is brighter and of earlier spectral type (K4/5).
210651981	C4	WDS 04285+1742	1.60	2004	...	$1.3(J)$		x		Binary resolved by Guenther et al. (2005) who report separation and magnitude difference

* "SB" indicates spectroscopic binary; † See text in Appendix A on this quadrupel system.

Foreman-Mackey D., Montet B. T., Hogg D. W., Morton T. D., Wang D., Schölkopf B., 2015, ApJ, 806, 215
Gallet F., Bouvier J., 2013, A&A, 556, A36
Gastine T., Morin J., Duarte L., Reiners A., Christensen U. R., Wicht J., 2013, A&A, 549, L5
Gliese W., Jahreiß H., 1991, Preliminary Version of the Third Catalogue of Nearby Stars. Tech. rep.
Guenther E. W., Paulson D. B., Cochran W. D., Patience J., Hatzes A. P., Macintosh B., 2005, A&A, 442, 1031
Hartman J. D., Bakos G. Á., Kovács G., Noyes R. W., 2010, MNRAS, 408, 475
Hartman J. D., Bakos G. Á., Noyes R. W., Sipőcz B., Kovács G., Mazeh T., Shporer A., Pál A., 2011, AJ, 141, 166
Hawley S. L., Davenport J. R. A., Kowalski A. F., Wisniewski J. P., Hebb L., Deitrick R., Hilton E. J., 2014, ApJ, 797, 121
Henden A., Munari U., 2014, Contributions of the Astronomical Observatory Skalnate Pleso, 43, 518
Herbst W., Mundt R., 2005, ApJ, 633, 967
Howell S. B. et al., 2014, PASP, 126, 398
Irwin J., Berta Z. K., Burke C. J., Charbonneau D., Nutzman P., West A. A., Falco E. E., 2011, ApJ, 727, 56
Jones E., Oliphant T., Peterson P., et al., 2001–, SciPy: Open source scientific tools for Python. [Online; accessed 2016-02-11]
Kawaler S. D., 1988, ApJ, 333, 236
Kiraga M., 2012, Acta Astronomica, 62, 67
Kopparapu R. K., 2013, ApJL, 767, L8
Kraus A. L., Ireland M. J., Hillenbrand L. A., Martinache F., 2012, ApJ, 745, 19
Lépine S., Gaidos E., 2011, AJ, 142, 138
Lépine S., Hilton E. J., Mann A. W., Wilde M., Rojas-Ayala B., Cruz K. L., Gaidos E., 2013, AJ, 145, 102
Luger R., Barnes R., Lopez E., Fortney J., Jackson B., Meadows V., 2015, Astrobiology, 15, 57
Lurie J. C., Davenport J. R. A., Hawley S. L., Wilkinson T. D., Wisniewski J. P., Kowalski A. F., Hebb L., 2015, ApJ, 800, 95
Mann A. W., Feiden G. A., Gaidos E., Boyajian T., von Braun K., 2015, ApJ, 804, 64
Mathur S., Salabert D., García R. A., Ceillier T., 2014, Journal of Space Weather and Space Climate, 4, A15
Matt S. P., Brun A. S., Baraffe I., Bouvier J., Chabrier G., 2015, ApJL, 799, L23
McCarthy C., Zuckerman B., Becklin E. E., 2001, AJ, 121, 3259
McQuillan A., Aigrain S., Mazeh T., 2013, MNRAS, 432, 1203
McQuillan A., Mazeh T., Aigrain S., 2014, ApJS, 211, 24
Montet B. T. et al., 2015, ApJ, 809, 25
Morrissey P. et al., 2007, ApJS, 173, 682
Morrissey P. et al., 2005, ApJL, 619, L7
Neuhäuser R., Sterzik M. F., Schmitt J. H. M. M., Wichmann R., Krautter J., 1995, A&A, 297, 391
Newton E. R., Charbonneau D., Irwin J., Berta-Thompson Z. K., Rojas-Ayala B., Covey K., Lloyd J. P., 2014, AJ, 147, 20
Newton E. R., Irwin J., Charbonneau D., Berta-Thompson Z. K., Dittmann J. A., West A. A., 2015, ArXiv e-prints
Nielsen M. B., Gizon L., Schunker H., Karoff C., 2013, A&A, 557, L10
Noyes R. W., Hartmann L. W., Baliunas S. L., Duncan D. K., Vaughan A. H., 1984, ApJ, 279, 763
Pallavicini R., Golub L., Rosner R., Vaiana G. S., Ayres T., Linsky J. L., 1981, ApJ, 248, 279
Penz T., Micela G., 2008, A&A, 479, 579
Pfeffermann E., Briel U. G., Freyberg M. J., 2003, Nuclear Instruments and Methods in Physics Research A, 515, 65
Pizzolato N., Maggio A., Micela G., Sciortino S., Ventura P., 2003, A&A, 397, 147
Press W. H., Rybicki G. B., 1989, ApJ, 338, 277
Ramsay G., Doyle J. G., Hakala P., Garcia-Alvarez D., Brooks A., Barclay T., Still M., 2013, MNRAS, 434, 2451
Rappaport S. et al., 2014, ApJ, 788, 114
Reid I. N. et al., 2004, AJ, 128, 463
Reiners A., Basri G., Browning M., 2009, ApJ, 692, 538
Reiners A., Joshi N., Goldman B., 2012, AJ, 143, 93
Reiners A., Mohanty S., 2012, ApJ, 746, 43
Reiners A., Schüssler M., Passegger V. M., 2014, ApJ, 794, 144
Rugheimer S., Kaltenegger L., Segura A., Linsky J., Mohanty S., 2015, ApJ, 809, 57
Saxton R. D., Read A. M., Esquej P., Freyberg M. J., Altieri B., Bermejo D., 2008, A&A, 480, 611
Scargle J. D., 1982, ApJ, 263, 835
Schlieder J. E. et al., 2016, ArXiv e-prints
Schrinner M., Petitdemange L., Dormy E., 2012, ApJ, 752, 121
Segura A., Kasting J. F., Meadows V., Cohen M., Scalo J., Crisp D., Butler R. A. H., Tinetti G., 2005, Astrobiology, 5, 706
Segura A., Walkowicz L. M., Meadows V., Kasting J., Hawley S., 2010, Astrobiology, 10, 751
Skumanich A., 1972, ApJ, 171, 565
Stassun K. G. et al., 2011, in Astronomical Society of the Pacific Conference Series, Vol. 448, 16th Cambridge Workshop on Cool Stars, Stellar Systems, and the Sun, Johns-Krull C., Browning M. K., West A. A., eds., p. 505
Stelzer B., Marino A., Micela G., López-Santiago J., Liefke C., 2013, MNRAS, 431, 2063
Vanderburg A., Johnson J. A., 2014, PASP, 126, 948
Vanderburg A. et al., 2016, ApJS, 222, 14
Vilhu O., 1984, A&A, 133, 117
West A. A., Hawley S. L., Bochanski J. J., Covey K. R., Reid I. N., Dhital S., Hilton E. J., Masuda M., 2008, AJ, 135, 785
West A. A. et al., 2004, AJ, 128, 426
West A. A., Weisenburger K. L., Irwin J., Berta-Thompson Z. K., Charbonneau D., Dittmann J., Pineda J. S., 2015, ApJ, 812, 3
Wright N. J., Drake J. J., Mamajek E. E., Henry G. W., 2011, ApJ, 743, 48
Zacharias N., Finch C. T., Girard T. M., Henden A., Bartlett J. L., Monet D. G., Zacharias M. I., 2013, AJ, 145, 44